Appraising Forgeability and Surface Cracking in New Generation Cast and Wrought Superalloys

M. FERNANDEZ-ALVAREZ, A. VAASUDEVAN, E. FISCHER, C. RAE, T. WITULSKI, and E.I. GALINDO-NAVA

Surface cracking poses a major problem in industrial forging, but the scientific understanding of the phenomenon is hampered by the difficulty of replicating it in a laboratory setting. In this work, a novel laboratory-scale experimental method is presented to investigate forgeability in new generation cast and wrought superalloys. This new approach makes possible appraising the prevalence and severity of surface cracking by mimicking the die chilling effects characteristic of hot die forging. Two high γ'-reinforced alloys are used to explore this methodology. A Gleeble thermo-mechanical simulator is used to conduct hot compression tests following a non-isothermal cycle, with the aim to simulate the cooling of the near-surface regions during the forging process. FEA simulations, sample geometry design, and heat-treatments are used to ensure the correspondence between laboratory and real-scale forging. A wide range of surface cracking results are obtained for different forging temperatures and cooling rates—proving the soundness of the method. Surprisingly, samples heated up to higher initial temperatures typically show more extensive surface cracking. These findings indicate that—along with the local mechanical conditions of the forging—die-chilling effects and forging temperatures are paramount in controlling surface cracking, as they dictate the key variables governing the distribution and kinetics of γ' formation.

https://doi.org/10.1007/s11661-023-07009-9

I. INTRODUCTION

NICKEL-BASED superalloys are widely employed in gas-turbines, where a main application is the production of turbine discs.[1,2] Turbine discs are normally manufactured of polycrystalline nickel-based superalloys *via* two processing routes: ingot metallurgy or powder metallurgy—both of which include forging steps. However, the forging of superalloys is particularly challenging owing to their high resistance to deformation up to very high temperatures.[3] Cast-and-wrought superalloys tend to have very narrow processing windows but can often be conventionally hot die forged.[2,4] Typically, they are forged below their γ' solvus temperature to prevent undesirable grain-growth, since primary γ' particles inhibit grain boundary motion through Zener pinning.[1,5,6] Conversely, highly reinforced grades cannot normally be hot die forged.[1,2] Instead, they require isothermal forging to avoid die chilling and adiabatic heating,[7–9] which significantly increases the processing costs, particularly when combined with powder metallurgy.

Recently, there has been a growing interest in the widespread use of high γ' content cast-and-wrought alloys, such as René 65, Udimet 720, and Udimet 720Li.[10–14] Alloy Inconel 718 (IN718) is still extensively employed in turbine and compressor discs, but its operation temperature is limited to 600 °C to 650 °C due to the coarsening of the γ' and γ'' phases and the formation of the deleterious δ phase.[10,11,14–17] High γ' content cast-and-wrought alloys aim to bridge the gap in temperature design space between Alloy 718 and P/M grades.[10] An ideal high γ' content cast-and-wrought alloy combines hot die forgeability with the highest γ' volume fraction possible. Udimet 720 is a high strength alloy reinforced by γ' precipitation and solid solution of Mo, W, Cr, and Co.[12] It is a versatile grade that shows a range of properties depending on thermo-mechanical processing, microstructural control, and grain size.[12,18–20] In fine-grained form it possesses competitive strength levels and a temperature capability of

M. FERNANDEZ-ALVAREZ, A. VAASUDEVAN, and C. RAE are with the Department of Materials Science and Metallurgy, University of Cambridge, Cambridge, CB3 0FS, UK. Contact e-mail: mf631@cam.ac.uk. E. FISCHER and T. WITULSKI are with the Otto Fuchs KG, 58540, Meinerzhagen, Germany. E.I. GALINDO-NAVA is with the Department of Materials Science and Metallurgy, University of Cambridge and also with the Department of Mechanical Engineering, University College London, London, WC1E 7JE, UK. Contact e-mail: e.galindo-nava@ucl.ac.uk

Manuscript submitted September 29, 2022; accepted February 9, 2023.

Article published online March 22, 2023

650 °C to 700 °C.[10,18,21] Efforts have also been devoted to developing new 718-type alloys, which would benefit from sluggish precipitation kinetics and a non-strengthening high-temperature phase (δ) for ease of hot working and grain refinement.[22] One such 718-type alloy is VDM 780.[22,23] This alloy was developed as an improved derivative of IN718 for higher service temperatures up to 750 °C for turbine disc applications. The alloy contains a γ matrix; a bimodal distribution of γ'-hardening phase; and a high-temperature phase primarily precipitated at the grain boundaries, with a structure composed of both δ and η phases.[24]

The hot die forgeability of medium and high γ' content cast-and-wrought alloys remains largely unexplored. These alloys sit at the edge of cast and wrought processability, have very narrow forging windows, and often show extensive surface cracking during hot die forging. Udimet 720 is difficult to forge, but previous studies indicate that it can be successfully forged *via* ring rolling, hot die forging, and superplastic isothermal forging.[10,19,25] Some authors have investigated the isothermal deformation of Udimet 720[12,19,26] and its variant Udimet 720Li.[27–30] but studies on its hot die forgeability, by means of mimicking die chilling, are sparse. Likewise, previous studies on the forgeability of VDM Alloy 780 are very limited.[23] Moreover, none of these studies focuses on the appearance of surface cracking during forging; this is despite the relevance of cracking both scientifically and in industrial practice, where it is a major cause for rejecting forged parts.[31]

The very limited number of studies on the hot die forgeability of cast-and-wrought alloys can be partially ascribed to the complexity of replicating industrial hot die forging through laboratory scale tests. This has been recently acknowledged by Hardy *et al.*[10] in their comprehensive review of the challenges for novel cast and wrought superalloys. Laboratory scale tests must be designed so that the microstructures, the thermal variables (temperatures, heating rates, and cooling rates), and the mechanical variables (stresses, strains, strain rates) of the specimens are representative of larger forgings. Accordingly, most research on the forgeability of these alloys is focused on their isothermal forging, mostly using processing maps.[32–36] However, processing maps are not readily adaptable to processes like hot die forging where the workpiece undergoes complex thermal cycles. For example, they cannot account for thermal transfer (die chilling) effects, or the dynamic evolution of γ' precipitates in nickel-based superalloys—both of which have been shown to be relevant to the hot forging of these alloys.[9,37,38]

This work aims to expand the understanding of forgeability and surface cracking for advanced cast-and-wrought alloys. To this end, a novel experimental method is devised to simulate the hot die forging of these alloys through small-scale laboratory tests; importantly, the method replicates surface cracking as observed in large scale forgings. The new method is tested on 2 alloys with markedly different microstructures, Udimet 720 and VDM 780, for validation and to establish their respective forging windows, including critical conditions for surface cracking.

II. EXPERIMENTAL PROCEDURE

A. *Materials*

Udimet 720 and VDM 780 material were employed for this work; the chemical compositions of these alloys are provided in Table I. The analysis mainly focuses in Udimet 720 and targeted results are presented for VDM 780 to validate the methodology.

The materials were made available by Otto Fuchs KG in the form of as-forged pancakes; three Udimet 720 pancakes and one VDM 780 pancake were produced. For Udimet 720, a round billet of diameter ~ 120 mm and height ~ 95 mm was upset (3:1) to produce a first pancake of height ~ 32 mm. Samples were cut from this pancake for microstructural analysis *via* scanning electron microscopy (SEM) and heat-treatments. The outermost and innermost regions were avoided as macroetching revealed that inhomogeneous deformation occurred in these areas. Thirty double cone and thirty circular cylinders were machined for thermo-mechanical testing from the two other pancakes. The double cone specimen shape was chosen to concentrate stress at the middle section ('equator') of the sample—where the diameter is largest—and induce and control the occurrence of cracks. The double cones measured Ø1 = 10 mm, Ø2 = 15 mm, and h = 15 mm—where Ø1 is the diameter at the base and the top surface, Ø2 is the maximum diameter (at the equator), and h is the height. The circular cylinders measured Ø = 10 mm and h = 15 mm. For VDM 780, only double cone specimens were employed.

B. *Heat-Treatments*

The Udimet 720 as-forged pancake was cut into smaller (~ 30 × 30 × 10 mm) sections with a Birkett Cutmaster Ltd. Aquacut power saw and a computerised numerical control (CNC) EDM machine. In turn, these sections were cut into 10 mm cubes using a Struers Accutom-5 precision cutting machine. The heat treatment of samples was performed in argon-backfilled quartz ampoules for 20 minutes or 4 hours at 1030 °C, 1060 °C, or 1100 °C. These temperatures were chosen based on previous studies on the subsolvus forgeability of Udimet 720;[12,38] NB the solvus temperature commonly reported in the literature for Udimet 720 is ~ 1143 °C to 1157 °C.[12,19,39] The heat treatment time of 4 hours was selected to represent typical industrial furnace times prior to forging. Due to the unavailability of industrial data, the sub-solvus solutionising time for Udimet 720Li reported by Gopinath *et al.*[40] is used as a proxy. The 20-minute heat treatment was selected as an intermediate step, and to ascertain whether this time suffices to achieve equilibrium. The latter consideration has implications for thermo-mechanical testing, as detailed in Section IV–A. All samples were swiftly water-quenched to preserve their microstructures for SEM examination. Following SEM analyses, the micrographs were processed with ImageJ to quantify the total area fraction of γ' ($f_{\gamma'}$), the area fraction of primary, secondary, and tertiary γ' ($f_{\gamma'p}$, $f_{\gamma's}$, $f_{\gamma't}$); as well as the

Table I. Nominal Composition of Udimet 720 and VDM 780 (wt pct)

Alloy	Cr	Co	Mo	W	Al	Ti	Nb	C	B	Zr	Ni
Udimet 720	17.9	14.7	3.0	1.25	2.5	5.0	—	0.035	0.033	0.03	Bal
VDM 780	18	25	3	—	2.1	0.2	5.4	—	—	—	Bal

average size of each population ($r_{\gamma'p}$, $r_{\gamma's}$, $r_{\gamma't}$). For VDM780, only the as-received microstructure was characterised, since the study of this alloy is primarily to validate the effectiveness of the new methodology, and other works in the literature have reported microstructure analysis of VDM780 at similar processing conditions.[41–43]

C. *Scanning Electron Microscopy*

The as-received and heat-treated specimens were prepared into SEM samples using standard metallographic preparation techniques using a semi-automatic grinder/polisher Saphir 560 and finishing with 1 μm diamond paste. Certain samples were electrolytically etched using a 10 pct phosphoric acid solution at ~ 3 V (γ-phase etchant). The microstructures of the specimens were examined with backscattered electrons (BSEs) and secondary electrons (SEs) using a field emission gun scanning electron microscope Zeiss Gemini SEM 300. SE imaging was performed with an acceleration voltage of 5 kV using an in-lens SE detector (I-L SED) and an Everhart Thornley detector (ETD). An annular backscatter detector (aBSD) was used for BSE imaging at 20 kV and working distances (WDs) of 4 to 6 mm.

For quantitative analysis and statistical modelling of cracking for the processed Udimet 720 thermo-mechanically tested samples, a Zeiss GeminiSEM 300 was used to obtain SE panoramic images. For each sample, ~ 10 × 30 individual SE images of magnification 100 times and a resolution of 4096 × 3072 pixels were acquired. These were stitched with Carl Zeiss SmartStitch software to high accuracy. The resulting panoramic images were split in two and post processed with ImageJ.

D. *Finite Element Analyses for Experimental Design*

Finite element analysis (FEA) was conducted to obtain the thermal and mechanical information necessary to design the experiments—specifically the cooling rates, strain rates, and deformation temperatures. The hot die forging of a model Udimet 720 turbine disc was simulated using FEA.

The model used to study the hot die forging of a turbine disc is depicted in Figure 1(a). It consists of a two-step closed-die forging process: the first step is termed 'pre-forging' and involves deforming a Udimet 720 pancake into an intermediate shape; in the second operation or 'forging', the resulting workpiece is deformed into its final shape. Subsequently, the workpiece is allowed to cool naturally for 3600 seconds. Heat is transferred between the workpiece, the dies, and the atmosphere; friction acts between the dies and the

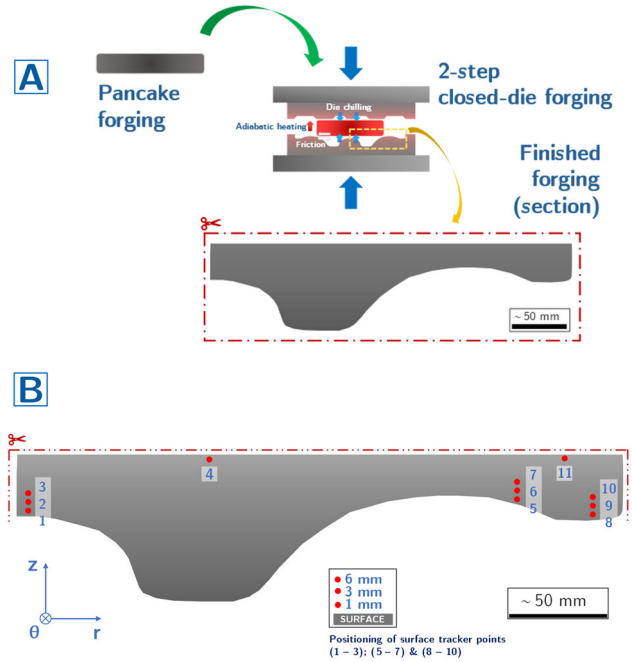

Fig. 1—(*a*) Schematic of the physical model used to simulate the hot die forging of a Udimet 720 turbine disc. (*b*) Schematic of the section of turbine disc analysed *via* FEA simulations. Points (1 to 11) designate the tracer points where data was simulated. The system of reference (r, θ, z) is shown at the bottom left of the figure.

workpiece. In both pre-forging and forging, the material is initially held at a homogenous temperature T_0 in the furnace prior to forging. Three nominal forging T_0 temperatures were chosen based on the same criterion as the heat-treatments (see Section II–B): 1030 °C, 1060 °C, and 1100 °C. The transfer of the workpiece from the furnace to the dies is simulated adding a 15 seconds lag where heat transfer occurs without deformation. The ram speed is constant of 15 mm/s.

The model was built into an FEA environment by Otto Fuchs KG using the commercial package FORGE®. The proprietary constitutive material data for Udimet 720 was obtained through isothermal tests. The results are assumed also to be approximately valid to determine the test matrix for VDM 780. To save computational costs, and since the workpiece is axisymmetric, only the 2D section highlighted in Figure 1(a) and shown in Figure 1(b) was simulated. FEA simulation data was collected at the 11 tracer points shown in Figure 1(b). Three sets of 3 tracer points each are placed at sections by the surface with different curvatures—these are designated as (1 to 3), (5 to 7), and (8 to 10). In addition, 2 tracer points (4, 11) are located at inner sections of the workpiece. The simulated data consisted

of temperature, strain, strain rate, and stress against time. For tensor and vector variables, the reference frame is shown in Figure 1(b); the coordinate functions (r, θ, z) correspond to the radial, tangential, and axial directions, respectively.

E. *Design of Experiments and Test Specimens*

A Gleeble thermal–mechanical simulator was used to mimic real scale metallurgical processing and determine the critical conditions that induce cracking. It served to correlate the effects of temperature, cooling rate due to die-chilling, and strain rate with the extent of cracking. Compression testing is preferred over tensile testing as forging is a compressive deformation process. It also allows attaining higher strains and the strain field becomes inhomogeneous during barrelling due to frictional effects, which is not the case in a tensile specimen, allowing to preserve the surface cracks for examination without material failure. However, it is important to realise that forging cracks are a manifestation of localised tensile stresses. Therefore, standard compression test pieces were redesigned with double cone shapes to have better control of surface tensile stresses at the sample edge that may lead to surface cracking. Details of sample geometry design and comparison with standard cylindrical test pieces are presented in the Appendix.

F. *Thermo-Mechanical Testing*

High temperature compression tests were performed with a Gleeble 3800-GTC thermal–mechanical simulation system at Delft University of Technology. Figure 2(a) shows a schematic of the testing system. The test specimens were subject to the thermo-mechanical cycle shown in Figure 2(b), which was designed to mimic real scale hot die forging. The rationale behind this cycle is developed in Section IV–A. First, they were rapidly heat up to different nominal forging temperatures (T_0): 1030 °C, 1060 °C, or 1100 °C for Udimet 720 or 950 °C, 990 °C, or 1030 °C for VDM 780. This was followed by a dwell step of 15 minutes to obtain temperature homogeneity and a representative microstructure across the sample. Subsequently, the samples were cooled down at different rates, between 0.1 °C/s and 30 °C/s, to a final or actual deformation temperature (T_f) of 880 °C (Udimet 720) or 860 °C (VDM 780). Cooling at rates $\leq$ 10 °C/s were achieved through natural cooling—reducing the heating input—whereas cooling at 30 °C/s necessitated air quenching. After a stabilisation dwell of 10 seconds to 20 seconds to reach temperature homogeneity, samples were deformed to strains of ~ 0.60 to 0.85 at a strain rate of 0.1 s^{-1}. Investigating the effect of the strain rate on forgeability is out of the scope of this study, yet it is expected that the strain rate correlates negatively with forgeability and positively with surface cracking. In other words, as the strain rate increases, forgeability decreases and more extensive surface cracking occurs. Finally, the specimens were air quenched to room temperature to freeze their microstructures for EM analysis. To minimise oxidation, all tests were conducted in vacuum. Prior to thermo-mechanical testing, all samples were heat treated for 4-hour at their respective nominal forging temperatures (T_0), followed by swift water quenching; this allowed obtaining

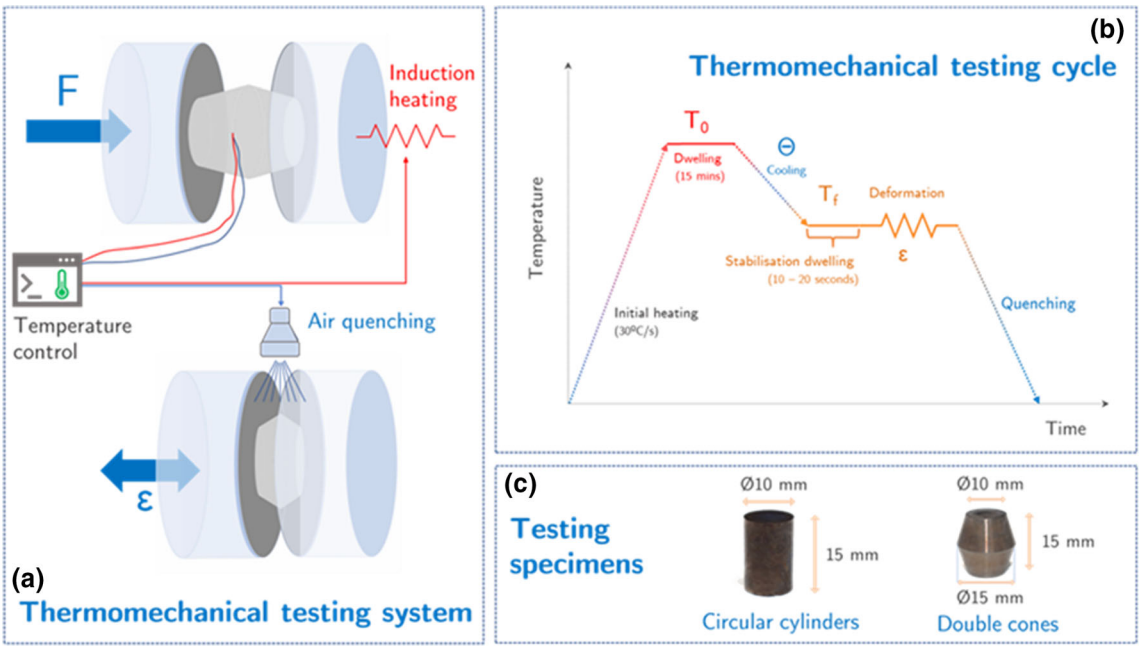

Fig. 2—(*a*) Schematic of the forging simulation system; (*b*) thermo-mechanical testing cycle employed to simulate hot die forging; (*c*) cylindrical and double cone specimens prior to testing.

microstructures representative of hot die forging using a dwell time of only 15 minutes (see Section IV–A).

To ensure appropriate induction heating, a thin oxide layer was removed by polishing the surface of the specimens with 2500-grit silicon carbide grinding paper. Before each test, an R-type thermocouple was welded to the centre of the specimen to measure the surface temperature. To reduce friction, anti-seizure nickel paste and graphite foil were applied between the specimen and the ISO-T tungsten carbide anvils. Following thermo-mechanical testing, specimens were visually inspected and classified qualitatively according to their level of surface cracking. Their final dimensions were measured with callipers; with this, a strain measurement was obtained which was compared to the strain figure provided by the Gleeble. Data series of temperature, force, stress, ram displacement, strain, strain rate, and time were obtained. The raw data was processed and visualised with OriginPro and Excel to ensure compliance.

III. RESULTS

A. *Microstructural Characterisation*

The SEM characterisation of Udimet 720 in the initial (as-forged pancake) condition is shown in Figure 3. The microstructure consists of γ' precipitates of various sizes in a γ matrix. Primary γ' (γ'_p) precipitates of ~ 1 μm, are present at the grain boundaries (Figure 3(a–c)). The interior of the grains is filled with fine secondary γ' (γ'_s) precipitates of ~ 100 nm (Figure 3(c), (d)). Globular geometries and precipitate splitting are observed for γ'_s, indicating partial ageing. No other phases are observed. Image analysis reveals that γ'_p precipitates occupy an area fraction of 17.42 pct and have a mean size of 3.37 μm, while γ'_s precipitates occupy an area fraction of 31.61 pct, and their mean size is 82.86 nm. In addition, regions of finer grains pinned by smaller γ'_p precipitates (mean size ~ 1.39 μm) are identified (Figure 3(e), (f)). Heaney *et al.*[14] reported similar structures in René 65 and stated that these are a carry-over from the billet microstructure where the volume fraction and composition of γ' are equivalent to other areas.

Figure 4 presents the SEM micrographs of VDM 780 in the as-received condition. Needle-shaped δ precipitates of size 2 to 4 μm are observed predominantly at the grain boundaries and twin boundaries, together with cuboidal γ' precipitates. The fraction of the δ phase could not be determined to high accuracy but was estimated to be ~5 pct. At an increased magnification, the sub-structure contained bimodal distribution of secondary and tertiary γ' precipitates. The area percentage of γ' was 26 pct with a mean particle size of 65 nm.

B. *Microstructure After Heat-Treatments*

Udimet 720 specimens were heat treated for 20 minutes or 4 hours at 1030 °C, 1060 °C, 1100 °C. The rationale behind these heat-treatment temperatures and times is detailed in Section II–B. Secondary electron SEM images of heat treated and γ-etched specimens are shown in Figure 5. γ'_p is observed at the grain boundaries in all low-magnification (Figures 5(a) through (f)) and medium magnification images (Figures 5(g) through (l)). For the 4 hours heat-treatments, $f_{\gamma'p}$ decreases modestly from 17.4 pct in as-forged condition to 13.7 pct at 1030 °C. As the temperature increases to 1060 °C and 1100 °C, it drops slightly further to 12.6 pct and 11.1 pct. γ'_p dissolution is even less significant for the 20-minute heat-treatments, with $f_{\gamma'p}$ = 13.3 pct at 1100 °C. γ'_p is consistently smaller in size after heat treatment, although substantial dispersion exists.

Significant γ'_s coarsening occurs upon heating by Ostwald ripening. This phenomenon is well documented for γ' precipitates in nickel-based superalloys.[44,45] Coarsened precipitates are visible at low magnification in the samples heat treated at 1030 °C for 4 hours (Figure 5(d)), 1060 °C for 20 minutes (Figure 5(b)) and 4 hours (Figure 5(e), and 1100 °C for 20 minutes Figure 5(c)) and 4 hours (Figure 5(f)). Medium and high magnification images (Figures 5(g), (m)) reveal that γ'_s also coarsens in the sample heat treated at 1030 °C for 20 minutes. Incomplete γ'_s coarsening is found in the samples heat treated for 20 minutes. In particular, the 1030 °C to 20 minutes sample (Figures 5(g), (m)) displays smaller and more numerous γ'_s precipitates than the 1030 °C to 4 hours one (Figures 5(j), (p)). The mean γ'_s particle size is 78 nm for 20 minutes *vs* 215 nm for 4 hours, and their area fractions 21.4 and 13.7 pct, respectively. The 1060 °C to 20 minutes sample (Figure 5(h)) shows a bimodal distribution of coarse and fine γ'_s. The average size of each population is 447 nm and 82 nm; their combined mean size is 99 nm and their combined volume fraction 18.4 pct. After 4 hours (Figures 5(e), (k), (q)) the fine γ'_s dissolves, and only the coarse particles remain. Their mean size increases to 289 nm and the volume fraction decreases to $f_{\gamma's}$ = 13.9 pct. γ' coarsening kinetics appear to accelerate at higher temperatures: the 1100 °C to 20 minutes sample (Figures 5(c), (i), (o)) contains very few γ'_s, and almost none are present after 4 hours (Figures 5(f), (l)). In all cases, γ'_s precipitates morph from quasi-cuboidal to spherical, with no signs of ageing. Interestingly, very finely dispersed γ'_t are observed in the 1100 °C to 4 hours sample (Figure 5(r)); they are believed to form during water quenching owing to the increased availability of dissolved γ' forming elements in the matrix. In this analysis, secondary γ' (γ'_s) refers to the unimodal distribution of intragranular γ' precipitates observed in the as-forged condition (Figures 3(c), (d)) and retained upon heat treatment. Tertiary γ' (γ'_t) denotes newly formed γ'—for example as described for Figure 5(r).

The γ'_s area fraction decreases as the heat treatment temperature increases. The decline in $f_{\gamma's}$ is particularly pronounced from 1060 to 1100 °C; at 1100 °C, almost all γ'_s dissolves. Similarly to the trend described for γ'_s particle sizes, the difference in $f_{\gamma's}$ between the 20 minutes and 4 hours heat-treatments is less significant at higher temperatures. At 1030 °C, $f_{\gamma's}$ is ~ 8 pct higher for the 20-min treatment, yet at 1100 °C that difference narrows to ~ 0.3 pct. Conversely, the fraction of

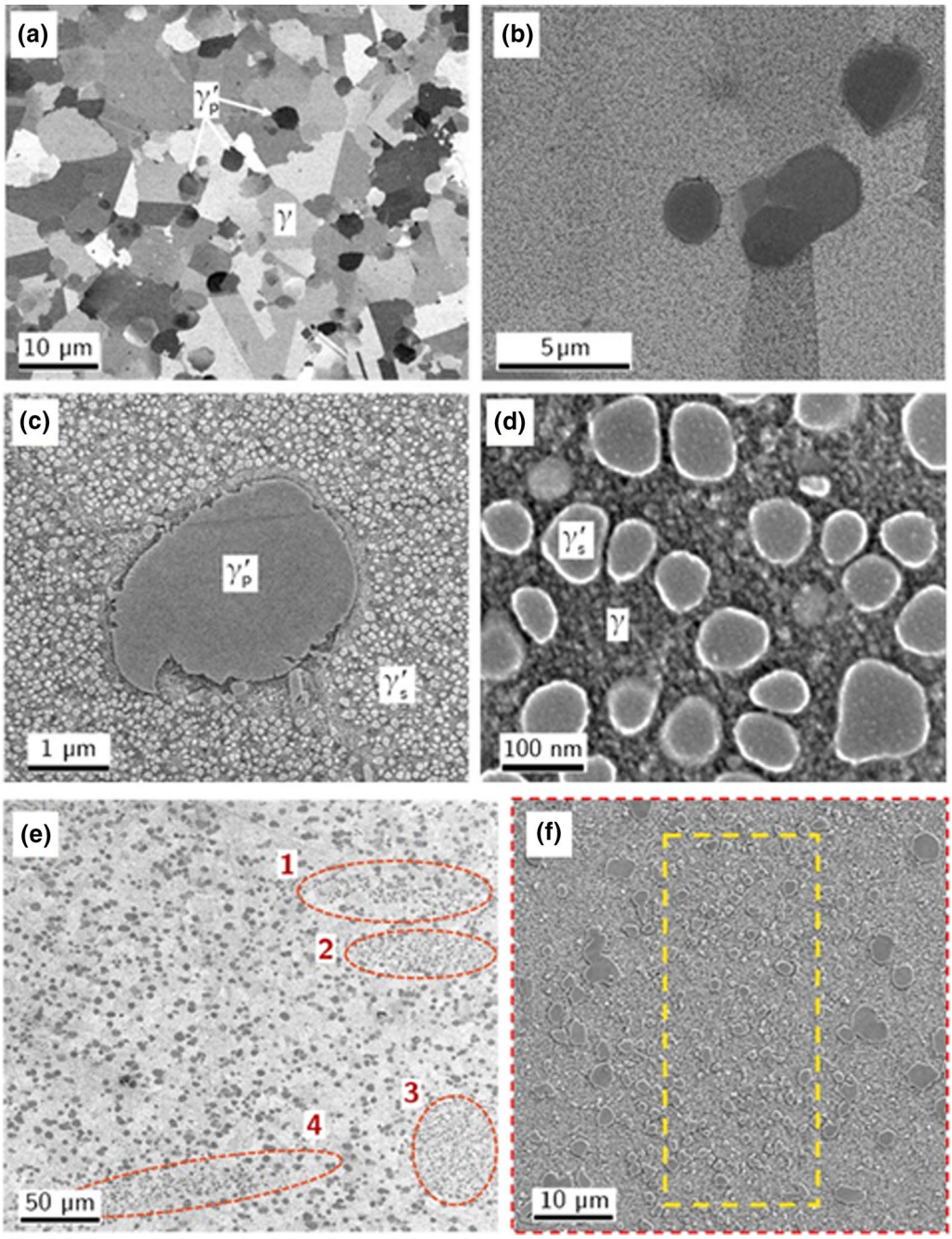

Fig. 3—BSE (*a*) and SE (*b* to *f*) SEM images of Udimet 720 material in initial (as-forged) state. Images of increasing magnification showing intergranular primary γ' (a to c) and intragranular secondary γ' (b to d) in a γ-matrix. NB the nanometric features observed between γ'_s particles in (d) correspond to topography in the γ-matrix due to γ-etching. (e) Regions of finer grains and finer primary γ' precipitates (1 to 4). (f) Higher magnification micrograph with one such area highlighted.

intergranular γ'_p ($f_{\gamma'p}$) decreases minimally in the 1030 °C to 1100 °C window; this is crucial on account of its grain-pinning function.

C. *Finite Element Analysis of Real Scale Forging*

1. *Temperature and cooling rate evolution*

Figure 6 shows temperature *vs* time during pre-forging (Figure 6(a)) and forging (Figure 6(b), (c)) for a nominal forging temperature (T_0) of 1100 °C. In both the pre-forging and forging steps, a distinct region is observed at $0 < t < 15$ seconds where the temperature decreases linearly. This corresponds to the transfer time between the furnace and the dies. Here, the cooling rate differs greatly across tracer points. During pre-forging, the temperature stays constant at the innermost tracer points (4) and decreases slightly (< 25 °C) at two of the three surface locations (sensors 5 and 8). By contrast, the temperature drops substantially at sensor 1. The latter undergoes cooling at a rate of 9.6 °C/s and reaches

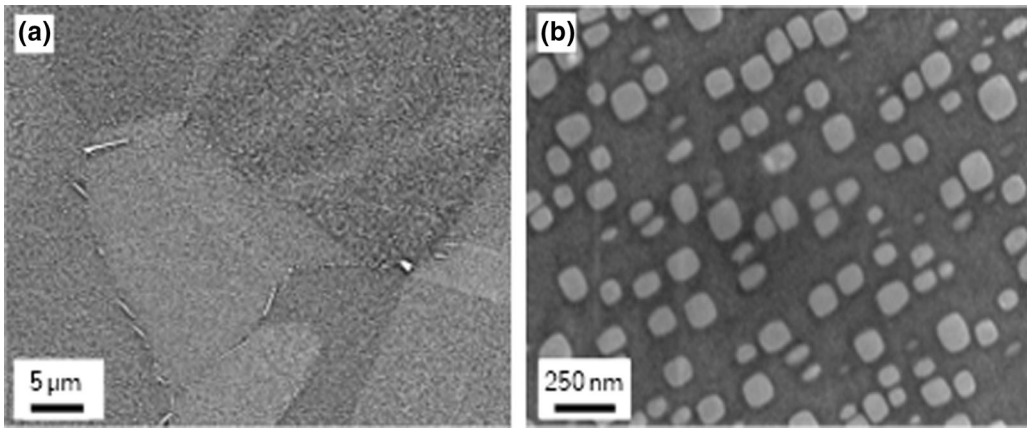

Fig. 4—(*a*) SE SEM micrograph of the as-forged VDM 780 material displaying needle-like grain boundary δ. (*b*) Higher magnification micrograph with cuboidal γ' precipitates.

~ 956 °C by the time deformation starts. In forging, the innermost sensors behave in the same way, but all three surface sensors (1,5, and 8) see cooling rates of ~ 1.5 °C/s and reach ~ 1075 °C prior to deformation. Analysis of the deformation paths (not shown in the figures) reveals that the ~ 400 pct difference in cooling rate at sensor 1 is due to the displacement of the sensors during deformation. Specifically, in pre-forging, sensor 1 is close to the surface and is subject to intense die chilling, whereas in forging it moved inwards and experienced slower cooling. Overall, these results indicate that the surfaces of the workpiece can cool down at rapid rates of up to − 10 °C/s during transfer operations.

Figure 6(c) shows a close-up view of Figure 6(b) for $t > 15$. This region corresponds to the deformation period, so both heat transfer and adiabatic heating occur. Like the transfer operation, there are substantial differences between tracer points. The temperature drop is most significant at the outermost sensors 1, 5, and 8 and diminishes with distance from the surface. Interestingly, the three innermost of the surface sensors 3, 7, and 10 (see Figure 6(b)) effectively see no cooling during forging ($t > 15$). This suggests that die chilling affects only a narrow band of material in contact with the dies. Furthermore, the temperature increase at the core of the workpiece (sensor 4) due to adiabatic heating outweighing heat transfer. A linear temperature drop is observed at the outermost surface sensors 1, 5, and 8 starting at ~ 16 seconds, ~ 18 seconds, and ~ 17 seconds, respectively. Their respective cooling rates obtained through linear regression are − 18, − 11.6 °C/s and − 10.3 °C/s. Thus, the largest temperature drop of ~ 60 °C happens at sensor 1. This linear regime is understood to begin when the workpiece and the die come into contact locally. The temperature stays nearly constant prior to the linear regime, confirming that significant workpiece cooling requires close proximity to the die.

A comparison of temperature evolution for forging temperatures (T_0) of 1030 °C, 1060 °C, and 1110 °C was completed, and only minor differences were found in the temperature gradients as the forging temperature decreases. The cooling rates decrease slightly at lower forging temperatures, but not enough to change the overall decrease in temperature. For example, the temperature drop seen by sensor 1 consistently remains ~ 60 °C. Additionally, and in light of Figure 6, henceforth only data of the outermost sensors 1, 5, and 8 are presented as illustrative of phenomena at the surface, and of sensor 4 to reflect the behaviour of the inner sections of the workpiece.

Temperature *vs* time data corresponding to the 3600 seconds cooling period subsequent to forging is shown in Figure 6(d)). In this case, the temperature drops more uniformly across tracer points. In addition, cooling is slower than during transfer or forging, with a fastest cooling rate of ~ 1 °C/s. Since no rapid temperature drops or significant stresses or strains happen upon cooling, this step is unlikely to affect forgeability or surface cracking. Hence, it is not considered in subsequent analyses.

2. *Strain and strain rate evolution*

The radial (ε_r), tangential (ε_θ), axial (ε_z), and shear (ε_{rz}) strain components corresponding to forging at T_0 = 1100 °C are shown in Figure 7. The shear strain components $\varepsilon_{r\theta}$ and $\varepsilon_{\theta z}$ are not shown since they are null for the entire domain. All strain components are bounded above by ~ 0.75 and below by—0.9. As expected, the axial strain is the greatest at most tracer points, although large radial and shear strains are also recorded at several locations. The tangential strain is generally lower and is bounded above by 0.4. Both tensile and compressive strains are seen across the workpiece for all except the tangential component, which stays consistently in tension. There appears to be a certain degree of symmetry of the radial and axial strains about the horizontal axis, whereby high tensile radial strains correlate with high compressive axial strains. The surface sensors (1, 5, and 8) largely display tensile radial strains and compressive axial strains, while no clear pattern is detected for shear. Sensor 5 shows the largest radial, axial, and shear strain; however, the tangential strain is highest at sensor 8. Remarkably, no clear tendency is identified for the innermost sensors (4) shifting from tensile to compressive radial, axial, and shear strains.

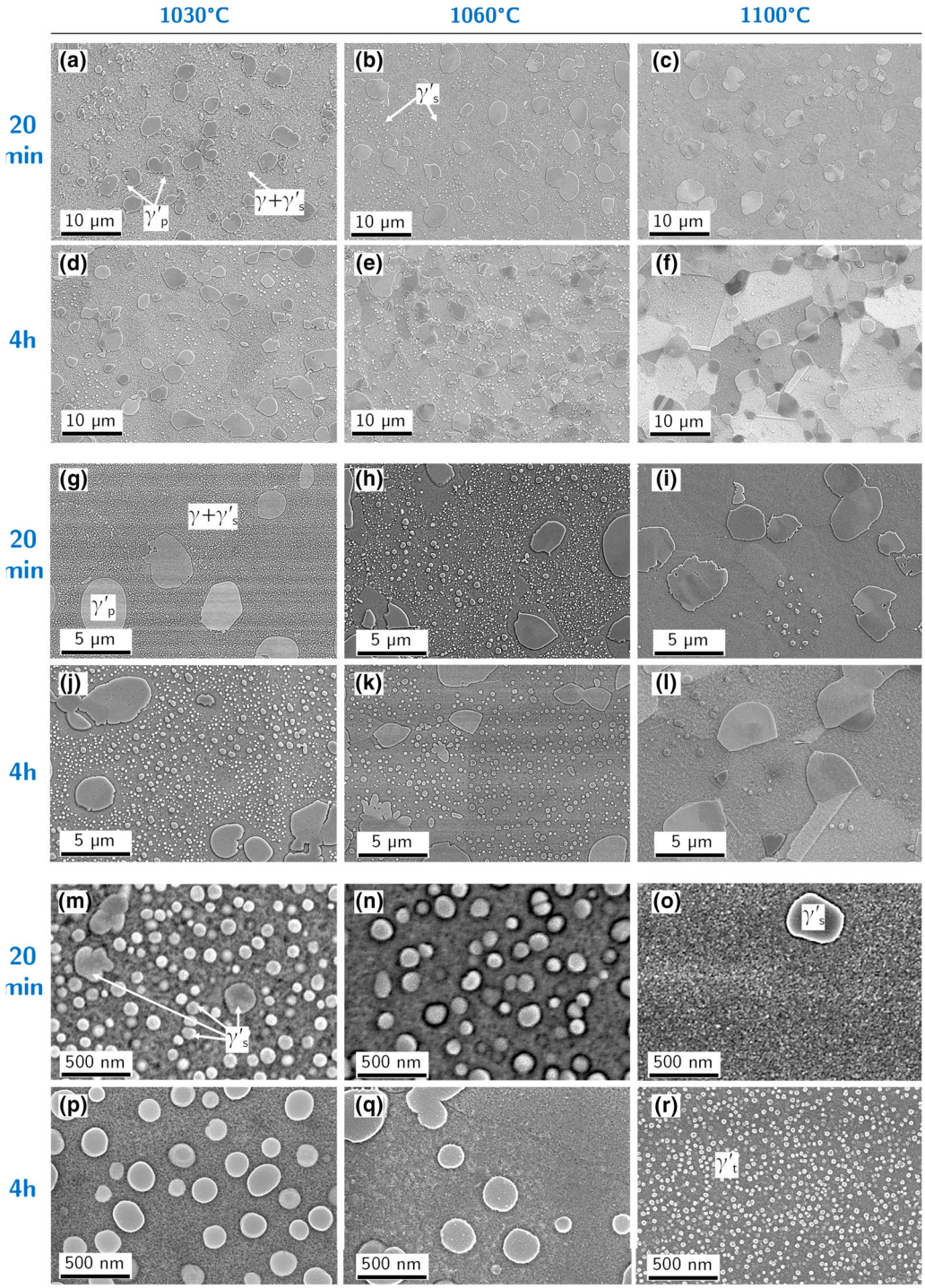

Fig. 5—SE SEM images of heat-treated Udimet 720 specimens at low magnification (*a*) through (*f*), medium magnification (*g*) through (*l*), and high magnification (*m*) through (*r*). Primary, secondary, and tertiary precipitates γ are labelled γ'_p, γ'_s, and γ'_t.

Although the geometry of the workpiece plays a major role in determining the deformation path during forging, certain differences between tracer points could be ascribed to thermal effects. In particular, there is a positive correlation between temperature and strain at sensors 4 (inner region) and 5 (surface). These sensors maintain the highest temperatures during deformation and are subject to the highest strains. However, this trend does not hold for sensors 1 and 8; this will be discussed further in the following section concerning stress distributions. The strain components for the remaining forging temperatures were also assessed but no marked variation with temperature was observed, and therefore the discussion of $T_0 = 1100$ °C can be extended to $T_0 = 1060$ °C and $T_0 = 1030$ °C.

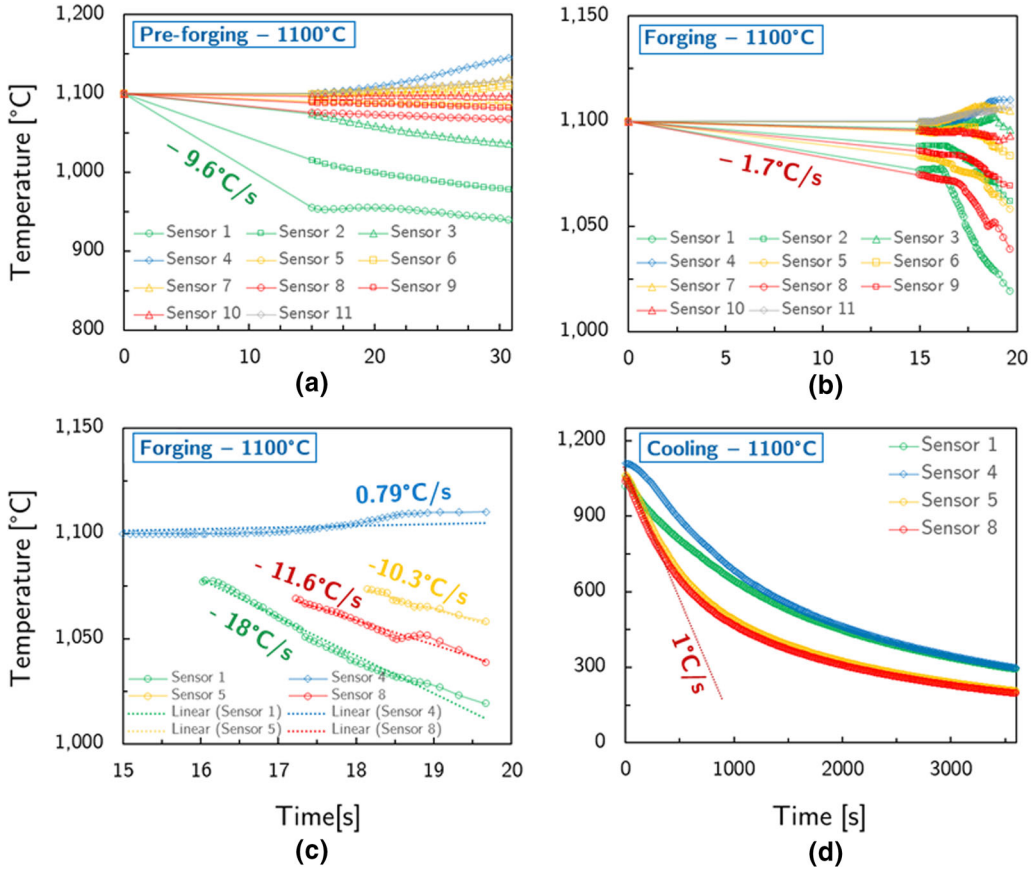

Fig. 6—Temperature *vs* time at: (*a*) sensors 1 to 11 for the pre-forging operation at $T_0 = 1100°$. (*b*) Sensors 1—11 for the forging operation at $T_0 = 1100$ °C. (*c*) Close up of (*b*) showing sensors 1, 4, 5, 8 during deformation ($t > 15$) and a linear regression model to obtain the cooling rates. (*d*) Temperature *vs* time at sensors 1, 4, 5, and 8 during cooling following forging at $T_0 = 1100$ °C; also plotted is a linear model of cooling at a rate of 1 °C/s. The dots represent the numerical (simulated) solution at each time step.

The strain rates during forging at different forging temperatures are plotted in Figure 7(e). The strain rates are obtained from the equivalent (von Mises) strain. Strain rates fluctuate around 0.1 s^{-1} and are bounded below by ~ 0.01 s^{-1} and above by ~ 1 s^{-1}. No dependence with temperature is noticeable for either forging or pre-forging, and no other clear trend is apparent.

3. *Stress evolution*

Figure 8 shows the time evolution of radial (σ_r), tangential (σ_θ), axial (σ_z), and shear (τ_{rz}) stress components at (a) $T_0 = 1030$ °C, (b) $T_0 = 1060$ °C and (c) $T_0 = 1100$ °C. The shear stress components $\tau_{r\theta}$ and $\tau_{\theta z}$ are not presented since they are null for the entire domain—as are their corresponding strains. At $T_0 = 1100$ °C, it is found that high normal stresses of up to ~ 1800 MPa exist across the workpiece. Shear stress attains more moderate values and is bounded below by – 100 MPa and above by 200 MPa. The normal stresses evolve similarly at all tracer points: a first quasi-steady regime in tension or low-stress compression is followed by a steep descent into compression. For radial stress, surface sensor 1 shows tensile stresses of ~ 150 MPa before shifting to compression. Sensor 5 sees low tensile stresses until ~ 18.5 seconds, when it starts exhibiting compression stresses of up to – 750 MPa. The tangential stress follows a similar pattern, although here sensors 5 and 8 display peaks of tensile stress in the initial regime. By contrast, the axile stresses stay consistently in compression or show negligible tension stresses in the quasi-steady region. Sensor 4 shows low stresses until ~ 18.5 seconds prior to displaying higher compression stress. Concerning shear stress, no clear pattern can be discerned. Examined together with the strain data (Figure 7), a clearer picture emerges of the thermal effect discussed above. Sensor 1 sees the highest stress and sensor 8 the lowest stress. Sensor 1 displays high stress and high strain in the normal directions, whereas sensor 5 shows comparatively low stress and even higher strains. Moreover, the temperature at sensor 1 is ~ 40 °C lower than at sensor 5. Hence, it appears that thermal effects are significant in determining the material's response, and even relatively modest temperature drops can cause notable hardening. Sensor 5 shows both low strain and low stress, which is attributed to the geometry of the workpiece.

As for the results at $T_0 = 1030$ °C and $T_0 = 1060$ °C, no qualitative difference is found between the three forging temperatures, although minor changes in stress amplitude occur. In particular, tensile radial and tangential stresses increase slightly at the surface sensors 1 and 8, but these stresses remain

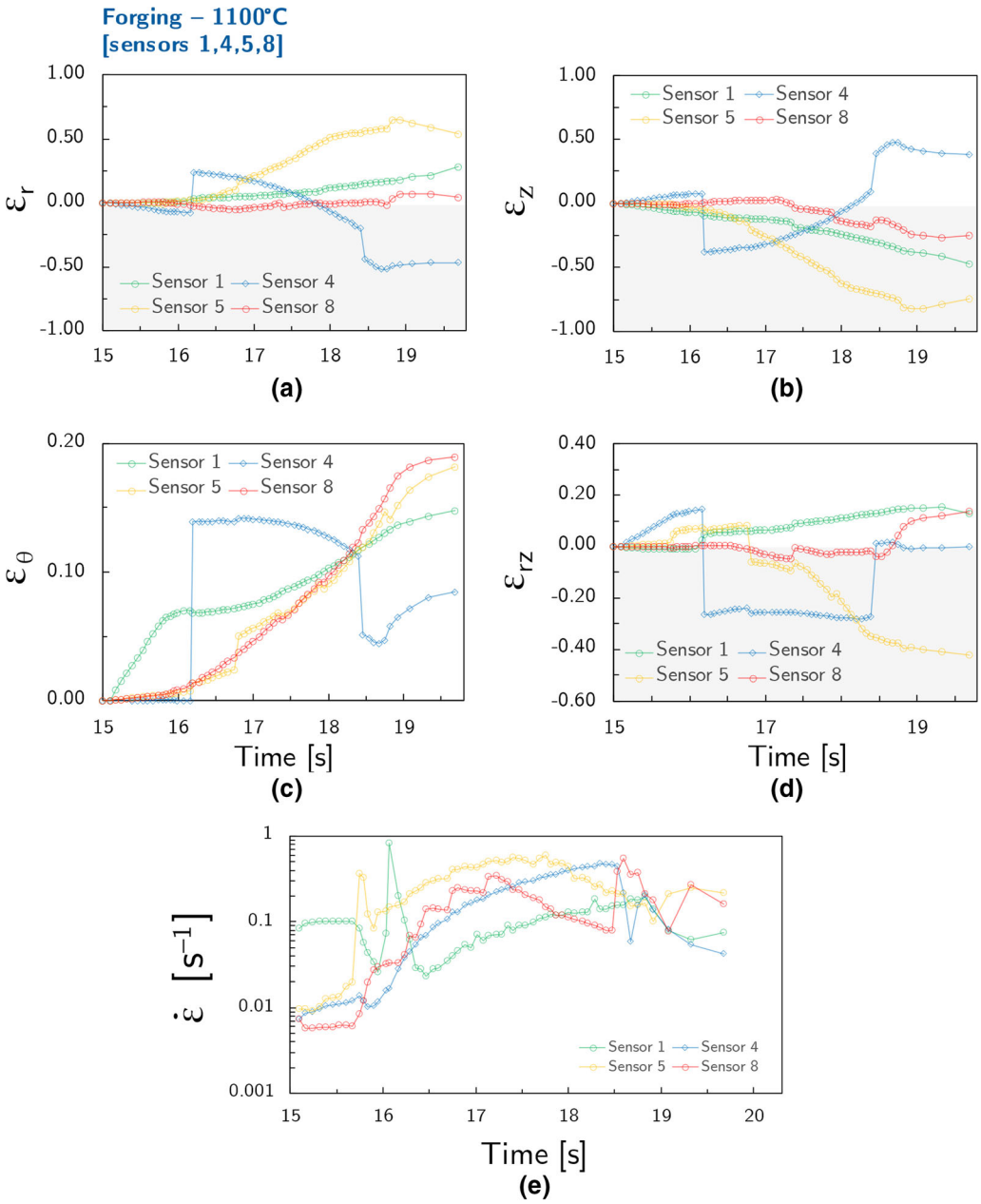

Fig. 7—(*a*) through (*d*) Strain components: (a) radial, (b) axial, (c) tangential, and (d) shear *vs* time at 1, 4, 5, and 8 only during forging at T_0 = 1100 °C. Positive values correspond to tension, and negative values to compression. (*e*) Strain rate *vs* time at sensors 1, 4, 5, and 8 during forging at T_0 = 1100 °C.

bounded above by ~ 215 MPa and ~ 350 MPa, respectively. Importantly, the observation that neither stresses nor strains change substantially with the forging temperature suggests that the thermal effects discussed above are caused by local and not global drops in temperature. In other words, as the temperature decreases locally, the flow stress increases, and deformation concentrates in sections of the workpiece where the temperature is higher.

It is noteworthy that these FEA simulations use constitutive data obtained empirically through isothermal tests. Thus, they do not capture the effect of die chilling on the microstructure and through it on the thermo-mechanical response of the material. This error is unlikely to compromise substantially the accuracy of the temperature results presented above, since the model incorporates direct heat transfer to the dies. Strain results can be affected; yet since the process is fundamentally strain controlled (the geometry of the dies and the ram speed are fixed), the largest inaccuracy is likely to come from the stresses. These results are hence approximative, but they show the trends of the relevant thermo-mechanical variables and provide range of values for the experimental design section that follows.

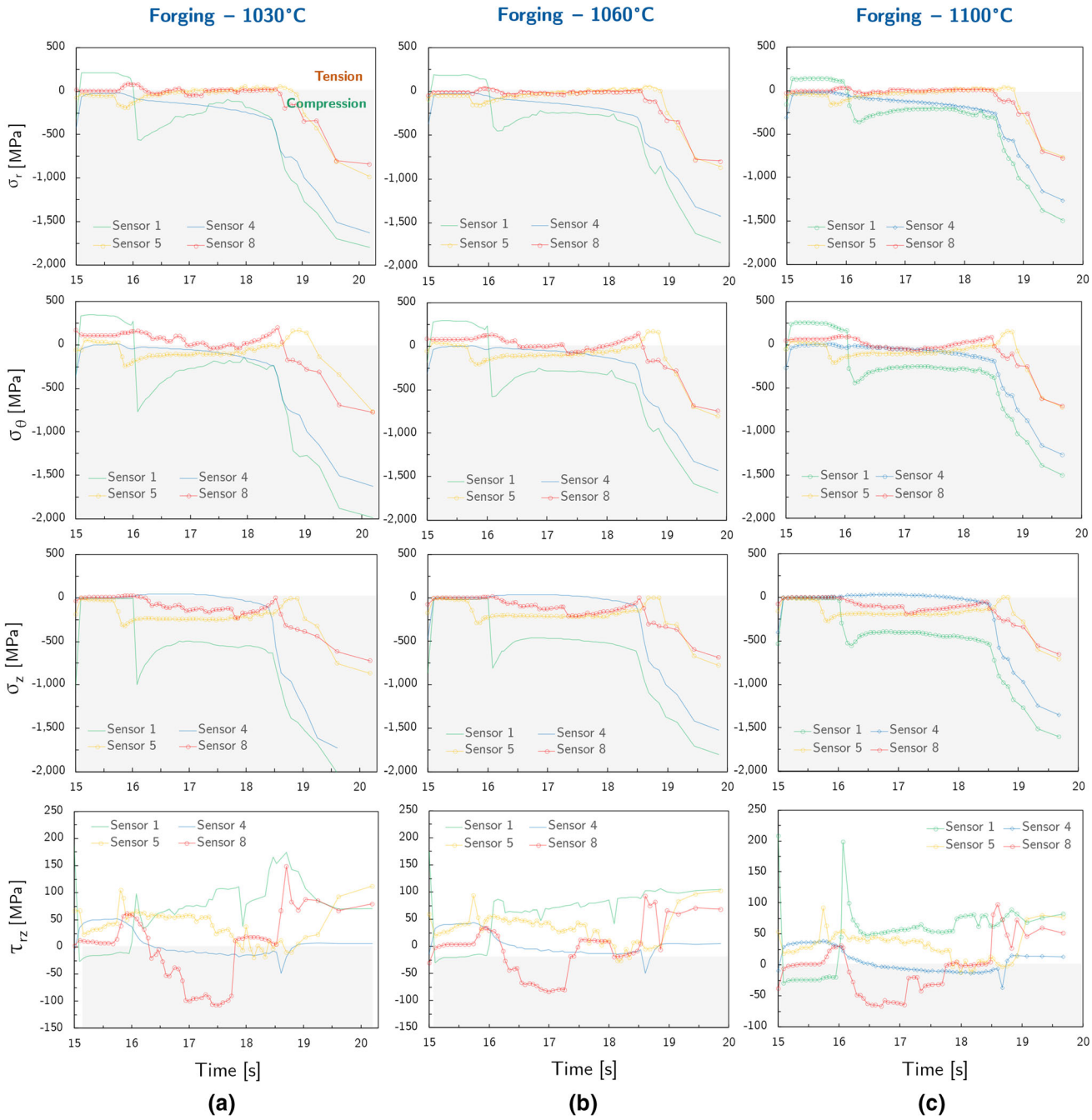

Fig. 8—Stress components (radial, tangential, axial, and shear) *vs* time during forging at: (*a*) 1100 °C, (*b*) 1060 °C, and (*c*) 1030 °C.

D. *Forging Simulation*

1. *Results for Udimet 720*

Figure 9 shows representative Udimet 720 double cones samples following thermo-mechanical testing at cooling rates of 1 °C/s, 10 °C/s, or 30 °C/s and nominal forging temperatures (T_0) of 1030 °C, 1060 °C, or 1100 °C. Successful outcomes were achieved for all nine conditions of this experimental matrix. A total of 26 double cone specimens were tested of which 18 are considered valid. Tests are considered valid if both the thermal cycle and the deformation characteristics are acceptably accurate. There exists moderate deformation inhomogeneity across the samples; this is most clearly observed in the (T_0, θ) = (1030 °C, 30 °C/s) condition, where the axial strain is slightly larger on one side of the sample.

Interestingly, a pattern is noted whereby the severity of cracking increases with both T_0 and the cooling rate; here severity of cracking refers to both the number of surface cracks and their depth. This challenges the idea that the alloy ought to be forged at temperatures below and close to its γ' solvus temperature (~ 1150 °C). In addition, it is observed that the nine specimens display varying degrees of surface cracking, ranging from no

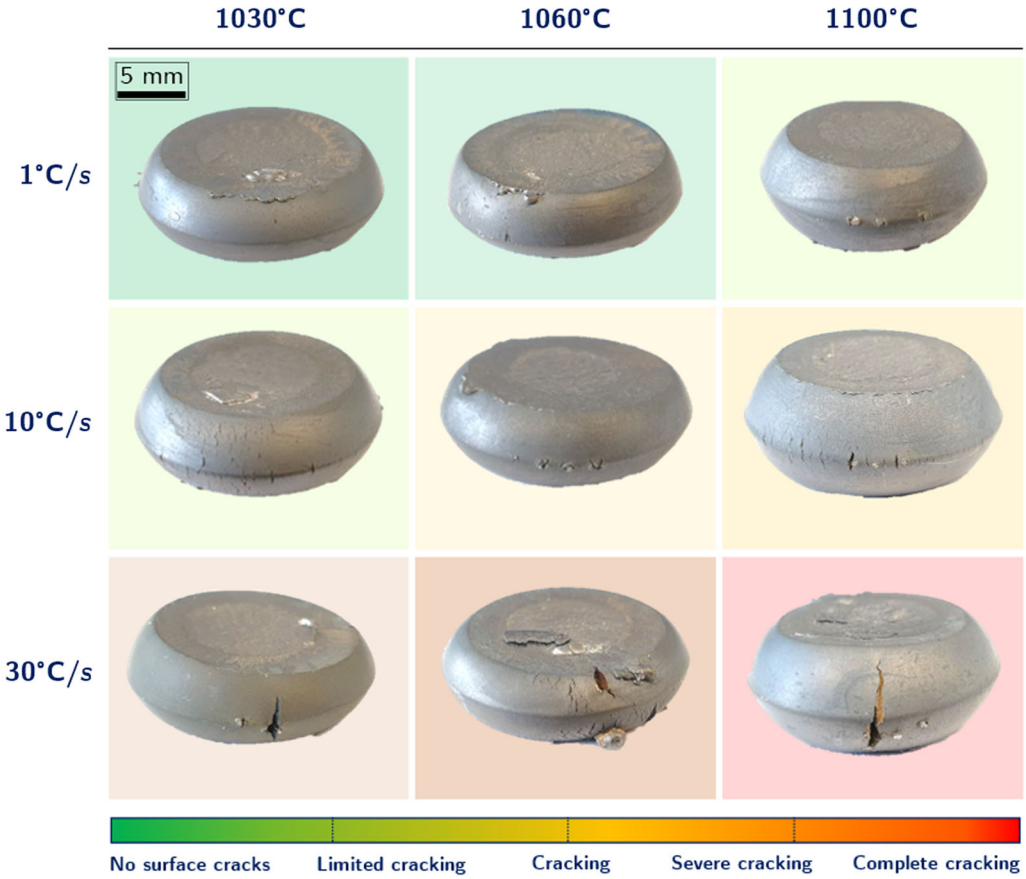

Fig. 9—Representative double cone samples of Udimet 720 tested at different nominal forging temperatures (T_0) and cooling rates (θ). The nominal forging temperature for each sample is indicated at the top of its column; the cooling rate is indicated at the left of its row. The background colour denotes the degree of cracking as per the gradient legend below (Color figure online).

cracks for the (1030 °C, 1 °C/s) sample to full cracking for the (1100 °C, 30 °C/s) condition. This demonstrates the soundness of the novel experimental method. Interestingly, surface cracking seems to be more sensitive to the cooling rate than to the T_0. Cracking is minimal for the slowest cooling rate of 1 °C/s irrespective of T_0, whereas at the medium cooling rate of 10 °C/s it is only significant for T_0 = 1100 °C. Conversely, all three samples cooled at 30 °C/s show substantial cracking. In particular, the (1030 °C, 30 °C/s) sample shows one large crack and the (1060 °C, 30 °C/s) sample an even distribution of large cracks. The (1100 °C, 30 °C/s) sample displays fracture with notable loss of material, and in the context of forging it can be considered to have failed catastrophically.

The full data corresponding to the double specimens is shown in tabular form in Table II. This includes the specimens shown in Figure 9 and the remaining 9 valid samples. Samples are designated by their true axial strain after deformation—obtained through calliper measurements and direct calculations. Although a fixed (nominal) strain of 0.8 was set on the Gleeble thermo-mechanical simulator, the actual results varied. Only samples with strains between 0.6 and 0.9 are considered valid. By definition, the full set of data displays the same patterns described for the representative samples of Figure 9: higher T_0 and especially higher cooling rates cause greater surface cracking. But in addition, there is a positive correlation between strain and surface cracking that is clearly seen in the (1060 °C, 30 °C/s) and (1100 °C, 10 °C/s) conditions. This behaviour is expected, but it is noteworthy that the axial strain appears to be a weaker indicator of surface cracking than T_0 or the cooling rate. For example, the thermo-mechanical testing of both (1100 °C, 30 °C/s) samples resulted in complete failure despite attaining relatively low-strain values.

Figure 10 shows representative thermo-mechanically tested cylindrical specimens of Udimet 720. Successful results are attained for 8 out the 9 intended conditions. The samples show varying degrees of surface cracking, providing additional backing for the effectiveness of the forging simulation methodology. They also behave equivalently to the double cones concerning T_0, cooling rates, and surface cracking. Consequently, they further question the notion that the forging window for the alloy lies below but close to its γ' solvus temperature. Surface cracking is negligible or marginal for the slowest cooling rate. For a cooling rate of 10 °C/s, samples with T_0 = 1060 °C display limited cracking, but when the T_0 increases to 1100 °C surface cracking appears. Severe cracking occurs for all three samples cooled at a rate of 30 °C/s. As in the double cones, catastrophic failure occurs for the (1100 °C, 30 °C/s) condition. Here again,

Table II. For All Double Cone Samples of Udimet 720 Tested at Different Nominal Forging Temperatures (T_0)—But Same Final Deformation Temperature (T_f)—and Cooling Rates (θ): Global Axial Strain (ε) and Degree of Cracking

θ	T_0		
	1030 °C	1060 °C	1100 °C
1 °C/s	$\varepsilon = 0.82$	$\varepsilon = 0.80$	$\varepsilon = 0.71$
10 °C/s	$\varepsilon = 0.74$	$\varepsilon = 0.75$	$\varepsilon = 0.62$ $\varepsilon = 0.63$
	$\varepsilon = 0.75$	$\varepsilon = 0.86$	$\varepsilon = 0.69$ $\varepsilon = 0.71$ $\varepsilon = 0.77$
30 °C/s	$\varepsilon = 0.82$	$\varepsilon = 0.69$ $\varepsilon = 0.82$ $\varepsilon = 0.86$	$\varepsilon = 0.63$ $\varepsilon = 0.67$
Udimet 720; $\varepsilon = 0.8$; $\dot{\varepsilon} = 0.1\ s^{-1}$; $T_0 = 880$ °C			

The degree of cracking is indicated by the background colour as per the gradient legend of corresponding Fig. 9

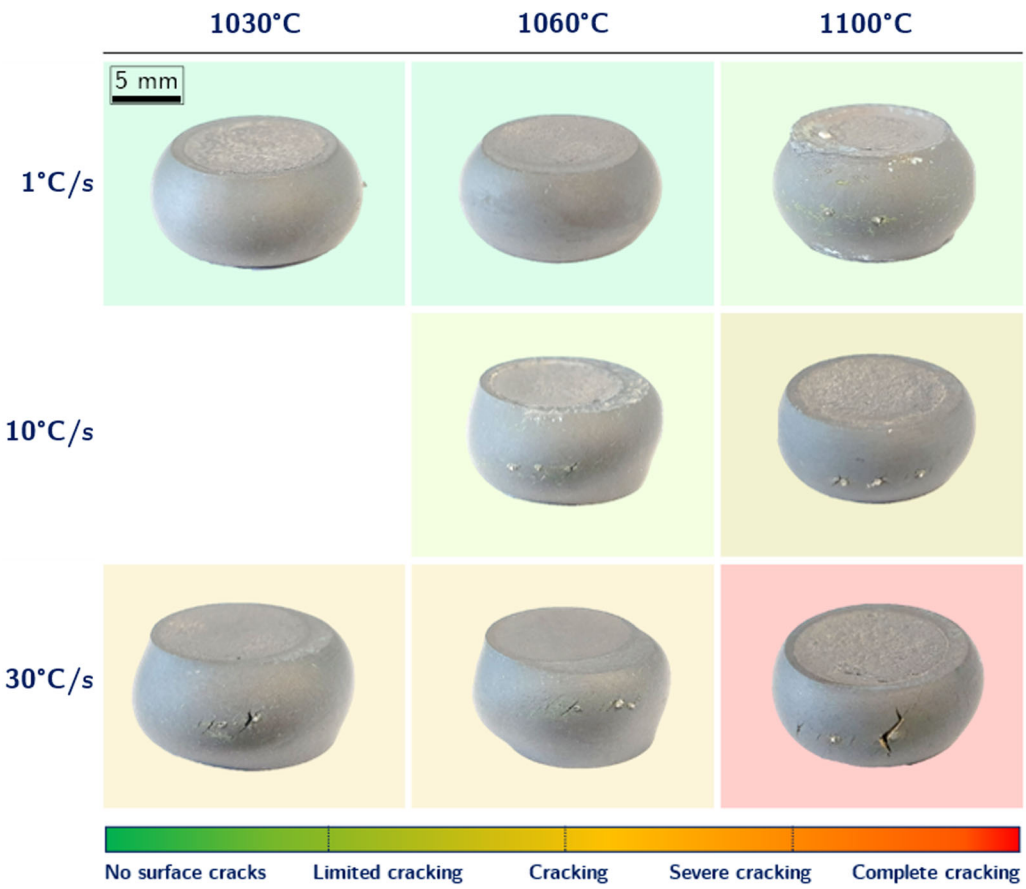

Fig. 10—Representative cylindrical samples of Udimet 720 tested at different nominal forging temperatures (T_0) and cooling rates (θ). T_0 for each sample is indicated at the top of its column; the cooling rate is indicated at the left of its row. The background colour denotes the degree of cracking as per the gradient legend below (Color figure online).

the cooling rate seems to affect cracking more than T_0. This is evidenced by the shift for $T_0 = 1100$ °C from no cracking at 1 °C/s to catastrophic failure at 30 °C/s. However, it is clear that T_0 also plays a significant role; for example, for a cooling rate of 30 °C cracking is much more limited at 1030 °C and 1060 °C than at 1100 °C.

Overall, 12 specimens of Udimet 720, from a total of 15 completed tests, are considered valid. Nevertheless, it is apparent from Figure 10 that deformation is more inhomogeneous than for the double cone specimens. Deformation inhomogeneities alter the local strain and stress states in the samples, thereby reducing accuracy.

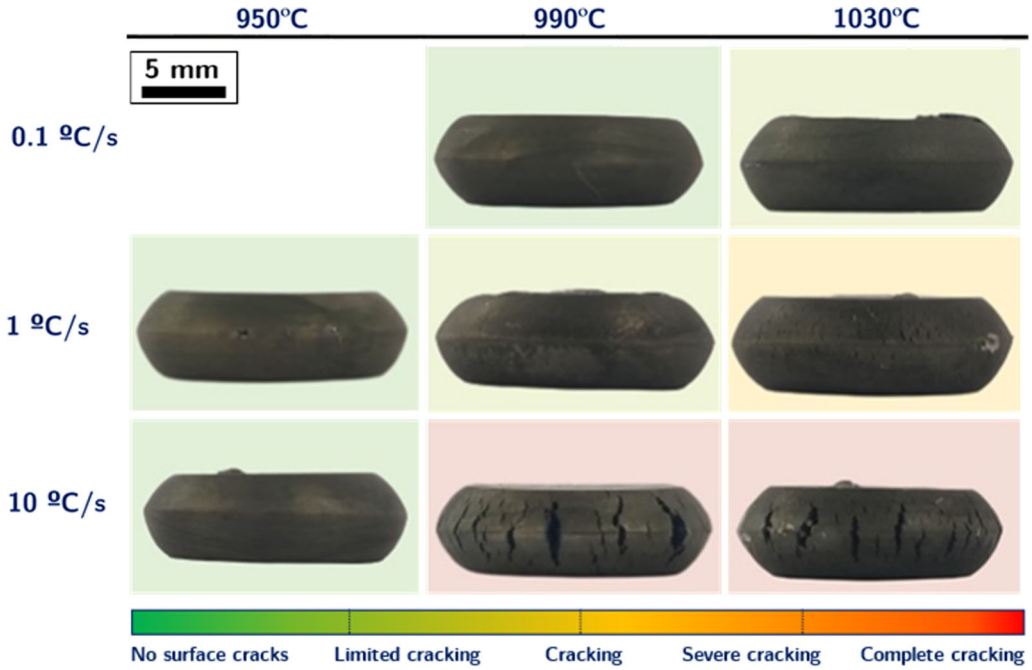

Fig. 11—Representative double cone samples of VDM 780 tested at different nominal forging temperatures (T_0) cooling rates (θ). The nominal forging temperature is indicated at the top of its column; the cooling rate is indicated at the left of its row. The background colour denotes the degree of cracking as per the gradient legend given below (Color figure online).

Besides, the cylindrical specimens show generally less surface cracking, which makes identifying patterns more difficult. This is due to the shortcoming that the compression of cylinders tends to produce lesser secondary tensile stresses, which are frequently behind surface cracking or cavitation. For these reasons, double cone specimens are prioritised in this research work, and only 15 cylindrical specimens are tested.

The full set of data corresponding to the cylindrical samples is shown in Table III. In addition to the observations noted for Figure 10, there is additional evidence that for each condition there exists a critical strain above which surface cracking is significant. This can be inferred from conditions (1060 °C, 10 °C/s) and (1100 °C, 10 °C/s), despite the limited number of samples. The critical strain can be thought of as a link between the macroscopic deformation variables (ε and σ) and the microstructural phenomena controlled by T_0 and θ. In effect, the critical strain correlates negatively with T_0 and the cooling rate. For example, a strain of $\varepsilon \sim 0.8$ for the (1060 °C, 1 °C/s) condition results in no cracking, for (1100 °C, 10 °C/s) limited cracking occurs, and for (1100 °C, 30 °C/s) it results in catastrophic failure.

2. *Results for VDM 780*

Thermo-mechanical tests on VDM 780 were conducted at T_0 = 950 °C, T_0 = 990 °C, or T_0 = 1030 °C and cooling rates of 0.1 °C/s, 1 °C/s or 10 °C/s**.** Since VDM 780 is a δ-forming alloy, the nominal forging temperatures were chosen to be in the regions where δ is also present to assess if other phases could affect the susceptibility of the alloy to surface cracking. The γ' and δ solvi for this alloy are, respectively, ~ 995 °C and ~ 1020 °C [41]. Therefore, the chosen temperatures were 950 °C, 990 °C, and 1030 °C—*i.e.,* below, at, and above the γ' solvus, with 1030 °C also being above δ solvus. In addition, these temperatures are consistent with recommended forging temperatures for δ-forming superalloys, such as Allvac 718plus,[46] which makes these conditions also industrially relevant. The cooling rates were chosen to be 0.1 °C/s, 1 °C/s, and 10 °C/s, so that: (A) the rapid cooling rate of 10 °C/s should avoid γ' precipitation during cooling from T_0 to T_f prior to deformation;[42] (B) the moderate cooling rate of 1 °C/s should just be suffice to trigger γ' precipitation during cooling; and (C) the slow cooling rate of 0.1 °C/s should lead to nucleation and significant growth of γ' precipitates during cooling from the solutionising temperatures prior to deformation. The lower values of cooling rates are also consistent with the lower testing temperatures (about 100 °C below) compared to Udimet 720, which sees higher cooling rates. Initial thermo-mechanical trials for VDM 780 at a strain rate of 0.1 s^{-1} were unsuccessful at various T_0 and cooling rates. Reducing the strain rate to 0.01 s^{-1} proved successful, indicating that the strain rate also plays a key role besides the aforementioned variables. For all subsequent forging simulation experiments, the strain rate was kept to 0.01 s^{-1}.

Figure 11 shows representative double cone samples tested at a T_f of 860 °C for different T_0 and cooling rates. A full range of cracking behaviour is observed. For T_0 = 950 °C the samples show no cracks for all cooling rates, whereas the 990 °C and 1030 °C samples show surface cracks at high-cooling rates. The

Table III. For All Cylindrical Samples of Udimet 720 Tested at Different Nominal Forging Temperatures (T_0) and Cooling Rates (θ): Global Axial Strain (ε) and Degree of Cracking

θ	T_0		
	1030 °C	1060 °C	1100 °C
1 °C/s	$\varepsilon = 0.79$	$\varepsilon = 0.82$	$\varepsilon = 0.70$ $\varepsilon = 0.82$
10 °C/s	N/A	$\varepsilon = 0.73$ $\varepsilon = 0.84$	$\varepsilon = 0.71$ $\varepsilon = 0.81$
30 °C/s	$\varepsilon = 0.72$	$\varepsilon = 0.71$	$\varepsilon = 0.70$ $\varepsilon = 0.82$
Udimet 720; $\varepsilon = 0.8$; $\dot{\varepsilon} = 0.1\ s^{-1}$; $T_0 = 880$ °C			

The degree of cracking is indicated by the background colour as per the gradient legend of corresponding Fig. 10

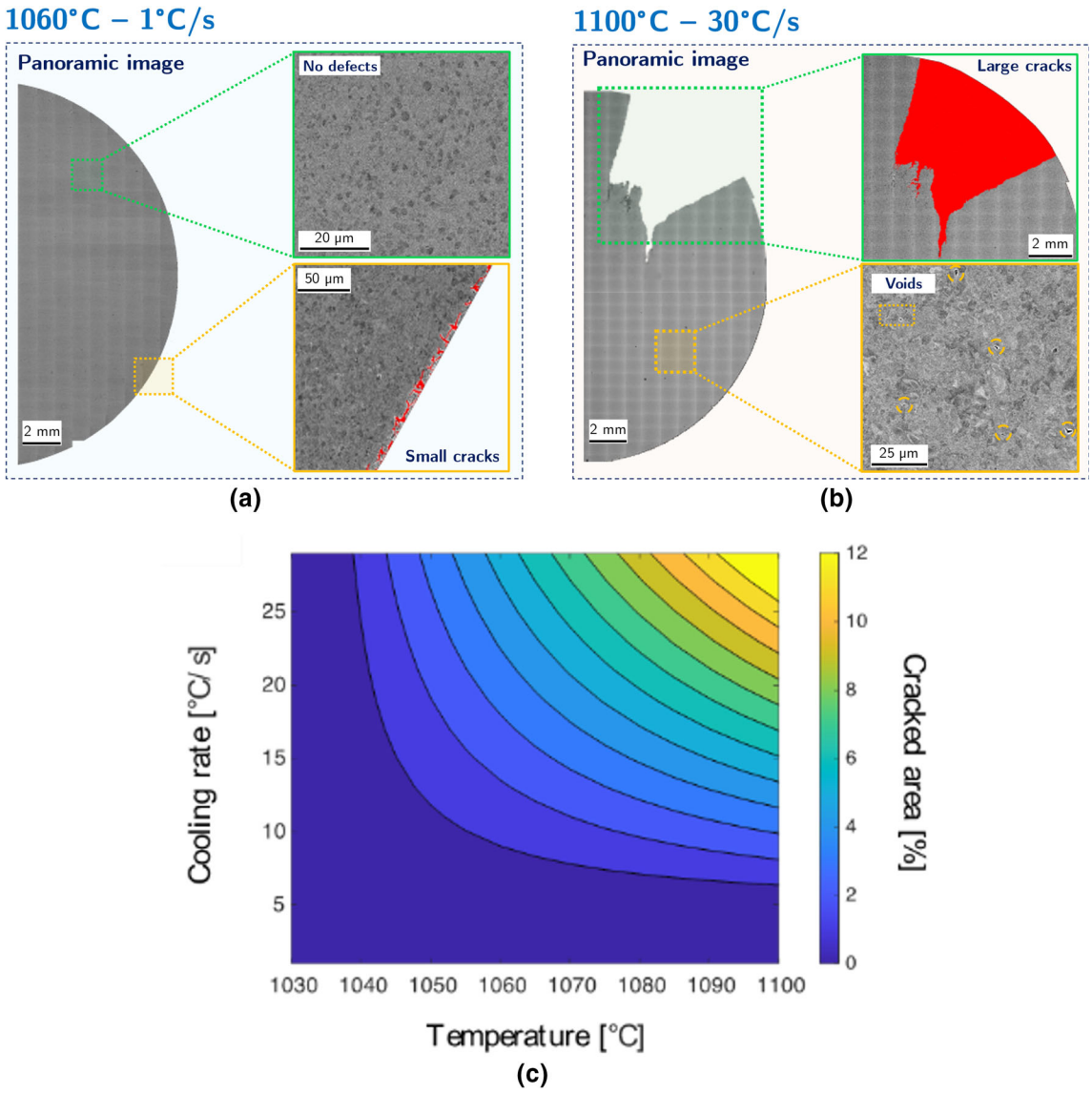

Fig. 12—(*a*), (*b*) Representative panoramic images showing close-ups of the inner and peripheral (edge) regions. (a) Sample was forged at 1060 °C and cooled down at 1 °C/s; it displays minimal surface cracking and no internal defects. (b) Sample was forged at 1100 °C and cooled at 30 °C/s; it shows significant loss of material and internal voids. (*c*) Contour plot of the multiple linear regression model for cracked area (pct) *vs* nominal forging temperature and cooling rate for Udimet 720 in the 1030 °C to 1100 °C temperature range and 0 °C/s to 30 °C/s cooling rate range.

conditions (990 °C, 10 °C/s) and (1030 °C, 10 °C/s) display full cracking and for commercial scale forgings could be assumed to have failed catastrophically.

The results indicate that for VDM 780—in agreement with Udimet 720—surface cracking is highly sensitive to T_0 and the cooling rate. They also suggest that the strain rate plays an important role in surface cracking. Moreover, these experiments further validate the soundness of the experimental method, which proved capable of replicating surface cracking during hot die forging for two significantly different alloy systems. In addition, the results corroborate the absence of cracks when both γ' and δ are retained (950 °C), and that the severity of cracking increases with the nominal forging temperature, *i.e.,* when both phases dissolve. This indicates—as with Udimet 720—that surface cracking is promoted by changes in γ' or δ (or both) upon cooling. However, further characterisation is required to elucidate the specific mechanisms of cracking in this alloy.

E. *Quantification of Cracking*

Figure 12 shows for Udimet 720 two panoramic images and close-ups in the peripheral and inner regions for two double cone specimens: (A) one for which no surface cracks are observed (1060 °C, 1 °C/s), and (B) another one which shows catastrophic failure (1100 °C, 30 °C/s). The macroscopic examinations and the qualitative classification set out above are a straightforward but effective approach to study forgeability and surface cracking. However, the method is limited in two aspects: first, macroscopic examinations do not show the depth of surface cracking, which is of the utmost importance in industrial practice; secondly, quantitative measurements are required to develop predictive statistical models. To the knowledge of the authors, no previous study has produced a robust procedure to quantify surface cracking, so a bespoke method was designed and employed. In brief, specimens were cut along their 'equator' and imaged *via* SEM. Then, the SEM micrographs were assembled into panoramic images, and image analysis was performed to measure the cracked surface area. Finally, the data was fed into a multiple linear regression model.

The panoramic images reveal the full extent of surface cracking. Image analysis confirms that for the samples classified as 'non-cracked' in the previous section, the crack surface area is negligible, whereas for the (1100 °C, 30 °C/s) condition it reaches ~ 16 pct—indicating a large loss of material. Surprisingly, low values (< 1 pct) were obtained for the (1030 °C, 30 °C/s) and (1100 °C, 10 °C/s) conditions; this is not in full agreement with the observations of Figure 9 and could indicate that cracks are highly superficial despite their seemingly large extension; another reason could be that the plane of view (equatorial plane) does not show the most severe cracks in all cases. Nevertheless, more measurements are needed before this can be affirmed this with confidence. The close-up images reveal that large surface cracking is accompanied by cavitation. A gradient of voids exists from the peripheral region, where the density of voids is maximum, to the inner region, where voids are sparser. Conversely, on the non-cracked samples voids are observed solely in the immediate surroundings of the edge.

A multiple linear regression model was built using the surface crack area measurements. The predictive model is given by Eq. [1], where the input variables are the nominal forging temperature (T_0) in [°C] and the cooling rate (θ) in [°C s^{-1}], and the response variable is the cracked area (κ). Figure 12(c) shows a contour plot of the model. The model reflects the tendencies regarding the relationship between cooling rate, temperature, and surface cracking. It also shows graphically the observation made above that the (1100 °C, 10 °C/s) experimental data point could be an outlier, as the model predicts significantly higher cracking areas (~ 3 pct) than were experimentally obtained (< 1 pct).

$$\kappa \sim 41.45 - 0.04\left[^{\circ}C^{-1}\right] T_0 - 8.95\left[s^{\circ}C^{-1}\right]\theta + 0.00865\left[s^{\circ}C^{-2}\right]T_0\theta \qquad [1]$$

IV. DISCUSSION

A. *Design of the Forging Simulation Method and Parameter Selection*

This work aims to develop an efficient and robust test method to replicate hot die forging on small-scale specimens for novel cast and wrought superalloys. The complexity of this task has been discussed above: for a laboratory test to be representative, it needs to reproduce the critical microstructures, thermal variables (temperatures, heating rates, and cooling rates), and the mechanical variables (stresses, strains, strain rates) of a real scale forging.

The method uses a Gleeble 3800-GTC thermal-mechanical simulation system to replicate hot die forging through compression tests on double cone and cylindrical specimens. The thermomechanical testing cycle (Figure 2(b)) is designed to simulate real scale hot die forging. In particular, the nominal forging temperature (T_0) is equivalent to typical furnace temperature in industrial hot die forging. The cooling step that follows aims at replicating die chilling effects on the surface of the forging, taking the temperature to the final or actual deformation temperature (T_f). Finite element analyses are used to estimate the evolution and distribution of the relevant variables in large scale forgings and feed into the forging simulation. Moreover, the method explores hot die forgeability in a broad sense—microstructure, flow stress, and defects—but is unique in that it is designed to target specifically the occurrence of surface cracking. FEA was employed to optimise the specimen geometry and ensure that the stresses and strains are representative of large-scale forging. The results demonstrate that the secondary tensile stresses that drive surface cracking are equivalent for the laboratory specimens and the real scale forgings.

Another crucial consideration is ensuring that the microstructures of the specimens prior to thermo-mechanical testing are equivalent to those of real scale forging. To attain representative microstructures, specimens are heat-treated prior to thermo-mechanical testing. Focusing on Udimet 720, the heat-treatments explored in Section III–B reveal that billet material does not attain equilibrium after 20 minutes at high temperature, but a steady state is achieved after 4 hours. In real scale hot die forging, workpieces are heated up in a furnace for hours to achieve temperature and microstructural homogeneity. However, holding samples at high temperature for hours is not feasible on a Gleeble 3800-GTC system: it is not technically sound for the apparatus and can introduce undesired deformation before the start of the tests. Heat-treatments allow reducing the dwelling time on the Gleeble to 15 minutes, which suffices to attain temperature homogeneity across the sample. The heat-treatments consist of holding the samples for 4 hours at their nominal forging temperature (T_0) followed by swift water quenching. In this way, microstructures are achieved where γ'_p and γ'_p are equivalent to real scale forging and any reprecipitating γ' exists as fine tertiaries. The presence of fine tertiaries is not considered problematic, since they readily dissolve during the 15 minutes dwelling step. Similarly and for consistency, VDM 780 specimens were also heat treated for 4 hours at their nominal forging temperatures.

In addition, the experimental design process required determining the parameters for testing Udimet 720 specimens. Specimens were forged at temperatures of 1030 °C, 1060 °C, or 1100 °C, and cooled at rates of 1 °C/s, 10 °C/s, or 30 °C/s. The strain and the strain rates were kept constant at 0.8 and 0.1 s^{-1}, respectively; the actual deformation temperature (T_f) is also kept constant at 880 °C. The rationale for these values is detailed below.

- The nominal forging temperatures (T_0) of 1030 °C, 1060 °C, and 1100 °C were selected within a prospective subsolvus forging window for Udimet 720, based on the limited literature available.[12,38] These match the forging temperatures (T_0) of the FEA simulations and those explored through heat treatments.
- The cooling rates of 1 °C/s, 10 °C/s, or 30 °C/s are chosen based on the FEA simulations on real scale workpieces. In these, cooling rates of 1 °C/s are recorded in the inner regions of the forging and ~ 10 °C/s by the surface. The cooling rate of 30 °C/s is selected based on preliminary trials with the Gleeble; this is the maximum cooling rate that can be reliably achieved with the instrument.
- The final or actual deformation temperature (T_f) of 880 °C is selected through a 'reasonable worst-case scenario' methodology. The largest temperature drop recorded through FEM simulations for real scale workpieces is ~ 150 °C corresponding to sensor 1 in pre-forging (see Figure 6). When this temperature drop is considered together with a T_0 of 1030 °C, a T_f of 880 °C results. For consistency, the final temperature is set at 880 °C for all three T_0 rather than subtracting 150 °C to each T_0.
- The strain of 0.8 derives from the FEA simulation of a real scale disc turbine, for which the maximum compressive strain (ε_z) is ~ 0.8.
- Likewise, the strain rate of 0.1 s^{-1} is selected based on the finite element analyses, as this the value around which strain rates fluctuate for the real scale forging.

It is noteworthy that the strain, strain rate, and final temperature could have been varied. However, early trials with the Gleeble showed that the deformation path and thermal evolution of the specimens are critically dependent on certain test conditions. For example, minor misalignments result in highly inhomogeneous deformation, and cooling at the highest rate (30 °C/s) not always yields the expected temperature control. Hence, a decision was made to prioritise two variables: the forging temperature and the cooling rate. This allowed obtaining a sufficient number of valid experiments despite the said hurdle. In general, these variables could be varied to get a more comprehensive picture of the forging map of an alloy.

As for VDM 780, similar strain and strain rate conditions were used, but the nominal forging temperatures and cooling rates were different. The rationale for this is discussed in Section III–D–2: lower temperatures than Udimet 720 were selected firstly to be consistent with the reported forging window for this Nb-containing alloy,[46] but also to study the possible influence of additional phases by forging in the regions containing $\gamma' + \delta$ (930 °C), δ (990 °C) and neither phase (1030 °C). As for the cooling rate, lower values than Udimet 720 were considered to be consistent with the lower forging temperatures and associated microstructural changes.

It is interesting to highlight that key similarities were found in both alloys, despite the range in nominal forging temperatures (T_0) being different by ~ 100 °C and the alloys having different initial microstructures. The severity of surface cracking increases with temperature, indicating that the extent of γ' dissolution at T_0 (and possibly δ) leading to re-precipitation at T_f should be connected to this damage mechanism. In addition, it was verified in the two alloys that severe surface cracking happens above a critical cooling rate between 1 °C/s and 10 °C/s, which supports the hypothesis that γ' dissolution and re-precipitation is closely linked to cracking. Based on the TTT diagram for VDM 780,[43] it can be inferred that a cooling rate of 10 °C/s avoids γ' precipitation during cooling, 1 °C/s may just be sufficient to trigger minor γ' precipitation, and the slow cooling rate of 0.1 °C/s promotes significant growth of γ' precipitates once T_f is reached. This implies that the dissolved (if any) γ' may re-precipitate during deformation (at T_f) for a cooling rate 10 °C/s, but less so for 1 °C/s and very little to none for 0.1 °C/s. In contrast for Udimet 720, which has faster kinetics and where the precipitation of γ' is likely to occur at all considered cooling rates, the increase in cracking severity at higher cooling rates could be related to the differences in

particle size distribution of the reprecipitated γ' phase. In summary, the present results provide evidence that the complex γ' kinetics during die chilling controls surface cracking to a great extent, yet further characterisation work is required to validate this hypothesis.

B. *Appraisal of the New Methodology*

The results presented in Section III–D demonstrate that the forging simulation methodology proposed in this work is effective and robust. About 70 tests of laboratory scale specimens provided 30 to 40 valid samples covering several combinations of forging temperatures, cooling rates and alloys. The novel method delivers a wide range of surface cracking states for Udimet 720 and VDM 780. Since the method is designed specifically to study the occurrence of surface cracking, the key evidence of its success is that it can reproduce on small scale specimens the surface cracking that has been reported to appear on large scale Udimet 720 workpieces under certain forging parameters. Double cone specimens are shown to be particularly robust for assessing susceptibility to surface cracking, confirming the importance of large secondary tensile stresses in cracking. Nevertheless, cylindrical samples also result in satisfactory outcomes.

From these results a reliable model can be built to find states of minimum cracking in the forging design space, for both industrial and scientific applications. The method is a significantly more efficient and economical approach of appraising hot die forgeability than conventional real scale trials. Acquiring comparable data through real scale trials would require testing different forging temperatures, performing several tests at each condition for repeatability, and—if possible—employing complex temperature measurement apparatus to measure cooling rates.

Despite the relevance of surface cracking in industrial forging, there exists very limited research on the subject. Recently, He *et al.*[31] investigated forging cracking in a bespoke P/M hot-extrusion nickel-based superalloy. They conducted isothermal compression tests and successfully replicated surface cracking in laboratory-scale tests. They found that a critical strain existed for each temperature and strain rate dyad, such that cracks emerged only when the strain exceeded it. However, this critical strain was lower than 0.4 for all conditions—a fairly low value. Indeed, all samples deformed at $\varepsilon = 0.7$ showed significant cracking. Conversely, the forging simulation results of this study show a wide range of cracking and non-cracking results depending on the cooling rate and processing temperatures, for both Udimet 720 and VDM 780. Specifically, for Udimet 720, forging to axial strains in excess of $\varepsilon = 0.8$ can result if no cracking at a low T_0 and cooling rate, whereas for a high T_0 and cooling rate severe surface cracking occurs for $\varepsilon = 0.7$. VDM 780 showed the same behaviour—corroborating the findings.

In addition, most studies on forgeability pertain to isothermal forging. Although some authors have indeed studied hot die forging[12] or conversion of cast ingot to billet stock,[38] a systematic method to study hot die forging was lacking—hence the relevance of the study. Finally, to the knowledge of the author, no published work on surface cracking of high γ' cast-and-wrought alloys exists to date. Therefore, the novel method paves the way for expanding the understanding of this phenomenon and, more broadly, hot die forgeability of these alloys.

The thermo-mechanical testing results robustly contest the notion that the optimal forging window for high γ'-reinforced cast and wrought lies below but close to the γ' solvus. Instead, they suggest that lower forging temperatures improve ductility and reduce surface cracking. For a constant deformation temperature (T_f), the severity of surface cracking increases with both the forging temperature and the cooling rate. Among these, cracking appears to be most sensitive to the cooling rate. These results are in agreement with the limited studies on the matter by Fahrmann and Suzuki[38] and Sczerzenie and Maurer,[12] which indicate that the ductility of Udimet 720 is substantially affected when specimens are annealed and subsequently cooled down to a lower testing temperature. Moreover, the experimental data indicates the existence of a critical strain above which surface cracks appear that is dependent on T_0 and θ. Quantitative data obtained *via* panoramic imaging and image analysis validates the findings outlined above, as does the multiple linear regression model built with this data. Extensive surface cracking is associated with the presence of a gradient of voids that is maximum in the peripheral regions and minimum at the core of the specimens. As for VDM 780, since it is a relatively new alloy, no similar studies concerning its forgeability and cracking behaviour were found in the literature. Hence, there was no data against which the results of this study could be compared; nonetheless, the fact that both alloys considered behave similarly provides confidence in the results obtained.

V. CONCLUSIONS

The following conclusions can be drawn from the present work:

- A novel experimental methodology was devised to simulate the hot die forging of high γ' content cast-and-wrought alloys, with a focus on surface cracking. The method uses a multi-step thermo-mechanical cycle on a Gleeble-3800 simulator to replicate the die chilling effects characteristic of hot die forging.
- FEA simulations were used to estimate the evolution of key thermo-mechanical variables during large scale forging of a turbine disc and feed these into the thermo-mechanical forging simulation method. FEA was employed to optimise the geometry of the testing specimens resulting in two geometries been used: cylinders and double cones.
- The method was successfully employed to investigate the forgeability of Udimet 720 and VDM 780. Specimens were tested at different forging temperatures and cooling rates and showed significant differences in surface cracking severity. Double cone

specimens were found to be more robust than cylindrical specimens; they also showed larger differences in surface cracking with forging temperatures and cooling rates, ascribed to the greater secondary tensile stresses. Panoramic imaging and image analysis were employed to quantify surface crack extension. Using the data obtained, a regression model was built to estimate surface cracking as a function of the forging temperature and cooling rate.

- The results indicate that surface cracking is highly sensitive to the forging temperature and the rate of cooling caused by die chilling. Interestingly, surface cracking severity increased with the forging temperature below γ' solvus, suggesting that complex γ' dissolution and re-precipitation during die chilling controls surface cracking. This disputes the current industrial practice and suggests that lower forging temperatures below $T_{\gamma' \text{ solvus}}$ improve forgeability.
- The method presented in this work and the determination of an optimal forging window, based on preventing surface cracking, for Udimet 720 and VDM780 have both industrial and scientific relevance. From an industrial point of view, this work paves the way for reduced material waste and increased environmental and cost efficiency. Scientifically, it provides a robust methodology to understand how the microstructure and forging parameters affect the occurrence of surface cracking. This also provides new insights into how to optimise superalloys for improved forgeability and mechanical performance.

CONFLICT OF INTEREST

On behalf of all authors, the corresponding author states that there is no conflict of interest.

APPENDIX

FEA was used to study Udimet 720 laboratory scale testing specimens to determine the optimal specimen geometry. Similar thermomechanical profiles were assumed for VDM 780. The physical model implemented in FEA is shown in Figure A1. Three geometries were studied: a cylinder, a truncated double cone ('double cone'), and a truncated double cone with a central cylindrical section ('cylindrical double cone'). They were compressed to a test (global) axial strain of 0.8, at a test axial strain rate of 0.1, and at various initial temperatures. Friction, adiabatic heating, and die chilling effects were included. The tungsten carbide anvils were initially set at a temperature of 550 °C based on industrial expertise. Tracer points where data sequences were recorded were located at the edge and the core of the specimens.

Figure A2 shows the radial, tangential, axial, and shear stresses against the corresponding strains at the edge and the core of cylindrical, double cone, and cylindrical double cone specimens forged at 1100 °C. Strain variations with time showed monotonic behaviour, hence they

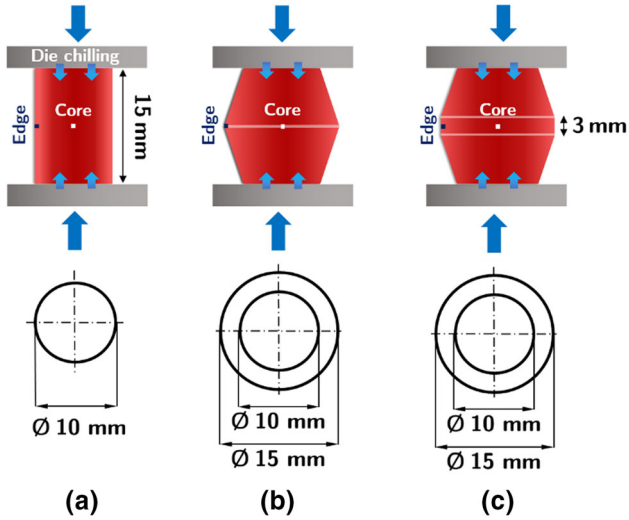

Fig. A1—Schematic of the physical model of laboratory-scale hot die forging tests. FEA simulations of the model were used to study the three geometries displayed: (*a*) cylinders, (*b*) double cones, and (*c*) truncated double cones.

are not shown. It is observed that the stress and strain distributions in the inner and peripheral regions are markedly different, whereas the divergence between different geometries is less significant. The radial stress is negligible at the edge and large (in compression) at the core, where it reaches ~ 550 MPa for both double cones and ~ 700 MPa for the cylinder. The tangential stress at the core behaves in the same manner. But at the edge, tangential tensile stresses of ~ 400 MPa exist. The axial stress behaves similarly, although there is a vertical shift downwards that causes a compression to tension transition at the edge. Both the shear stress and strain are negligible. Comparing the three geometries, the largest stress divergence between the cylinder and the double cones corresponds to radial stress at the core. At the edges, although they attain generally similar stress values, the cylinder does so at higher strain values. Interestingly, the double cone displays significantly lower axial stress at the edge than the cylindrical double cone, but for all variables considered, this is the only major difference between these two geometries. Since no substantial difference was found between the double cones and the cylindrical double cones, the former were selected on the basis of ease of manufacturing.

Figure A3 displays maps of the normal stresses corresponding to a (A) cylinder and (B) double cone specimen at the end of deformation. The shear stress is negligible and thus not shown (see Figure A2). A transition from tensile to compression stress is observed for all three normal stresses in both cases. Specifically, the radial component is compressive in the central regions of the sample and tensile in the peripheral regions. Interestingly, the stress gradient for the double cones is less steep which indicates that cracking could be less sensitive to deformation heterogeneities and shape changes, *i.e.*, cracking will likely be more localised at the edge of the sample, whereas crack initiation regions in the cylinder could be more heterogeneous and sensitive to the sample's final shape induced by barrelling. Therefore, the analysis that

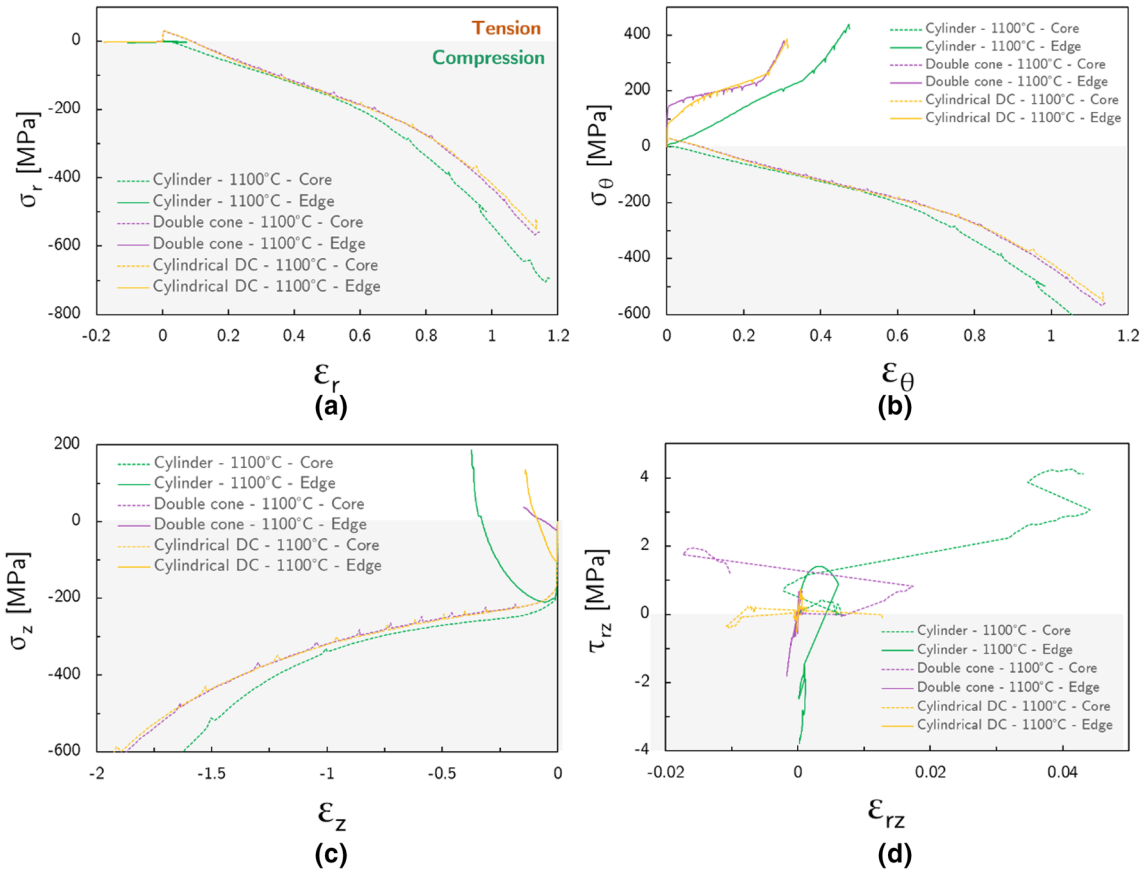

Fig. A2—Stress components *vs* corresponding strains for cylindrical, double cone, and cylindrical double cone samples forged at 1100 °C: (*a*) radial stress; (*b*) tangential stress; (*c*) axial stress; (*d*) shear stress. NB the radial stress curves for the core of the samples in (a) overlap at a stress of ~ 0 MPa. Data modelled at the core and the edge of the samples.

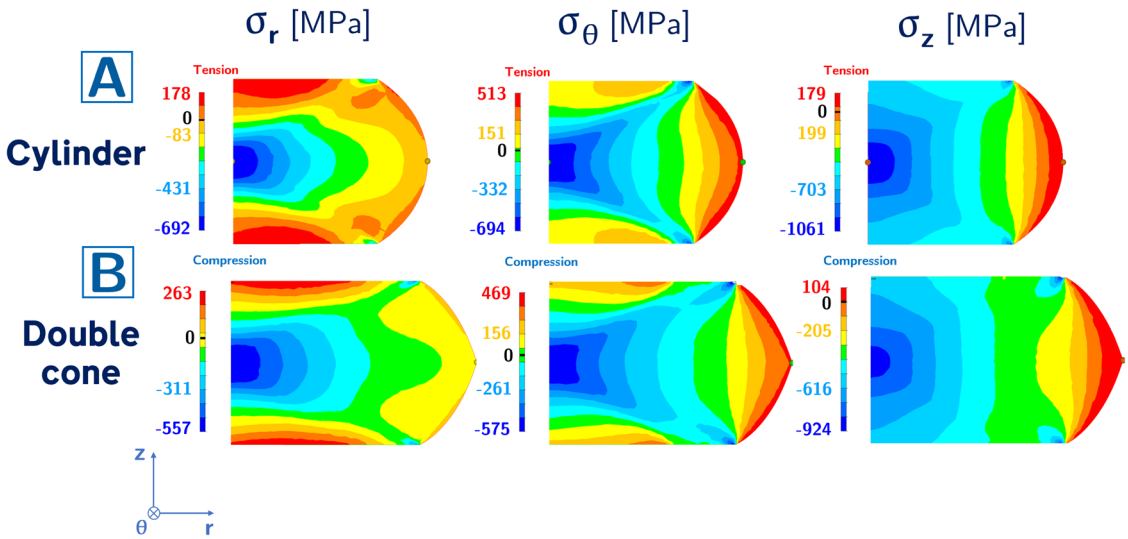

Fig. A3—Normal stress (radial, tangential, axial) maps corresponding to the forging of double cone specimens at a temperature 1100 °C. The tracer points shown at the middle section indicate where the core (left) and edge (right) data is recorded.

follows will focus on the results of the double cone specimens. A maximum tensile stress of ~ 180 MPa appears at the top and bottom surfaces, which are in contact with the dies. The tangential strain exhibits a pattern characteristic of upset cylindrical specimens: an 'x-shaped' region of high compressive stress that peaks at the core, a region of low stress (dead-metal zone) around it, and moderate tensile stress at the top and bottom

surfaces. In addition, a gradient of increasing tensile stress towards the lateral surfaces is observed that peaks at ~ 500 MPa. This is similar to the axial strain, which increases radially from ~ 1100 MPa in compression at the core to ~ 180 MPa in tension at the edge. Overall, Figures A2 and A3 confirm that the compression testing of cylindrical and double cone specimens provides a distribution stresses and strains comparable to those occurring at the surface of a real scale turbine disc, as per Section III–C. And in particular, they show secondary tensile stresses—which are crucial to replicate the surface cracking that can occur in real scale forging.

OPEN ACCESS

REFERENCES

1. R.C. Reed: *The Superalloys: Fundamentals and Applications*, Cambridge University Press, Cambridge, 2008.
2. M.J. Donachie and S.J. Donachie: *Selection of Superalloys for Design*, Wiley, Hoboken, 2002.
3. R.M.F. Jones and L.A. Jackman: *JOM*, 1999, https://doi.org/10.1007/s11837-999-0007-9.
4. H. Monajati, M. Jahazi, R. Bahrami, and S. Yue: *Mater. Sci. Eng. A*, 2004, vol. 373, pp. 286–93.
5. C.P. Blankenship, M.F.F. Henry, J.M. Hyzak, R.B. Rohling, E.L. Hall, C.P. Blankenship Jr., M.F.F. Henry, J.M. Hyzak, R.B. Rohling, and E.L. Hall: *Superalloys*, 1996, vol. 1996, pp. 653–62.
6. J. Chen, P. Zhang, J. Dong, M. Zhang, and Z. Yao: *Mater. Trans.*, 2015, vol. 56, pp. 1968–76.
7. T. Ohno, R. Watanabe, T. Fukui, and K. Tanaka: *Trans. Iron Steel Inst. Jpn.*, 1988, vol. 28, p. 958. https://doi.org/10.2355/isijinternational1966.28.958.
8. US6,908,519B2: 2005.
9. T. Altan, G. Ngaile, and G. Shen: *AMS Int.*, 2005, vol. 1, p. 1.
10. M.C. Hardy, M. Detrois, E.T. McDevitt, C. Argyrakis, V. Saraf, P.D. Jablonski, J.A. Hawk, R.C. Buckingham, H.S. Kitaguchi, and S. Tin: *Metall. Mater. Trans. A Phys. Metall. Mater. Sci.*, 2020, vol. 51, p. 2626. https://doi.org/10.1007/s11661-020-05773-6.
11. A. Devaux, B. Picqué, M.F. Gervais, E. Georges, T. Poulain, and P. Héritier: *Superalloys 2012*, Springer, New York, 2012.
12. F.E. Sczerzenie and G.E. Maurer, 2012, pp. 573–80.
13. A. Devaux, E. Georges, and P. Héritier: Adv. Mater. Res., 2011.
14. J.A. Heaney, M.L. Lasonde, A.M. Powell, B.J. Bond, and C.M. O'Brien, in *8th Int. Symp. Superalloy 718 Deriv. 2014*, 2014, pp. 67–77.
15. J.F. Radavich: 2012, pp. 229–40.
16. C.Y. Lin, H.Y. Bor, C.N. Wei, and C.H. Liao: in *Materials Science Forum*, vol. 941, Trans Tech Publ, 2018, pp. 2167–72.
17. A. Kracke, 2016, pp. 13–50.
18. S.B. Kim, A. Evans, J. Shackleton, G. Bruno, M. Preuss, and P.J. Withers: *Metall. Mater. Trans. A Phys. Metall. Mater. Sci.*, 2005, vol. 36, pp. 3041–53.
19. H. Monajati, M. Jahazi, S. Yue, and A.K. Taheri: *Metall. Mater. Trans. A Phys. Metall. Mater. Sci.*, 2005, vol. 36, p. 895. https://doi.org/10.1007/s11661-005-0284-z.
20. H. Hattori, M. Takekawa, D. Furrer, and R.J. Noel, 2012, pp. 705–11.
21. M. Goto and D.M. Knowles: *Eng. Fract. Mech.*, 1998, vol. 60, pp. 1–8.
22. J. Rösler, T. Hentrich, and B. Gehrmann: *Metals (Basel)*, 2019, vol. 9, pp. 1–20.
23. J. Sharma, M.H. Haghighat, B. Gehrmann, C. Moussa, and N. Bozzolo: *Superalloys 2020*, Springer, New York, 2020, pp. 450–60.
24. T. Fedorova, J. Rösler, J. Klöwer, and B. Gehrmann: *MATEC Web Conf.* https://doi.org/10.1051/matecconf/20141401003.
25. Allegheny Technologies Incorporated (ATI): *ATI 720 Alloy Technical Data Sheet*. Pittsburgh. 2014.
26. J.M. Hyzak, R.P. Singh, J.E. Morra, and T.E. Howson: in *Superalloys 1992*, ed. by S. Antolovich, R. Stusrud, R. MacKay, D. Anton, T. Khan, R. Kissinger, and D.L. Klarstrom (TMS, The Minerals, Metals &Materials Society, 1992), pp. 93–101.
27. Z. Wan, L. Hu, Y. Sun, T. Wang, and Z. Li: *J. Alloys Compds.*, 2016, https://doi.org/10.1016/j.jallcom.2018.08.010.
28. J.G. Wang, D. Liu, T. Wang, and Y.H. Yang: *Adv. Mater. Res.*, 2014, vol. 887, p. 15.
29. F. Liu, J. Chen, J. Dong, M. Zhang, and Z. Yao: *Mater. Sci. Eng. A*, 2016, vol. 651, pp. 102–15.
30. Q.Y. Yu, Z.H. Yao, and J.X. Dong: *Mater. Charact.*, 2015, vol. 107, pp. 398–410.
31. G. He, F. Liu, L. Huang, and L. Jiang: *Adv. Eng. Mater.*, 2016, vol. 18, pp. 1823–32.
32. Z. Jia, Z.X. Gao, J.J. Ji, D.X. Liu, T.B. Guo, and Y.T. Ding: *Rare Met.*, 2021, vol. 40, pp. 2083–91.
33. H. Zhang, K. Zhang, Z. Lu, C. Zhao, and X. Yang: *Mater. Sci. Eng. A*, 2014, vol. 604, pp. 1–8.
34. G. He, F. Liu, J. Si, C. Yang, and L. Jiang: *Mater. Des.*, 2015, vol. 87, pp. 256–65.
35. Y. Kong, P. Chang, Q. Li, L. Xie, and S. Zhu: *J. Alloys Compds.*, 2015, vol. 622, pp. 738–44.
36. Y. Ning, Z. Yao, H. Guo, M.W. Fu, H. Li, and X. Xie: *Mater. Sci. Eng. A*, 2010, vol. 527, pp. 6794–99.
37. S.L. Semiatin, D.W. Mahaffey, N.C. Levkulich, O.N. Senkov, and J.S. Tiley: *Metall. Mater. Trans. A Phys. Metall. Mater. Sci.*, 2018, https://doi.org/10.1007/s11661-018-4896-5.
38. M. Fahrmann, and A. Suzuki: in *Proceedings of the International Symposium on Superalloys*, 2008.
39. K.R. Bain, M.L. Gambone, J.M. Hyzak, and M.C. Thomas: *Superalloys*, 1988, vol. 1988, pp. 13–22.
40. K. Gopinath, A.K. Gogia, S.V. Kamat, R. Balamuralikrishnan, and U. Ramamurty: *Metall. Mater. Trans. A Phys. Metall. Mater. Sci.*, 2008, vol. 39, pp. 2340–50.
41. C. Solís, J. Munke, M. Bergner, A. Kriele, M.J. Mühlbauer, D.V. Cheptiakov, B. Gehrmann, J. Rösler, and R. Gilles: *Metall. Mater. Trans. A Phys. Metall. Mater. Sci.*, 2018, vol. 49, pp. 4373–81.
42. M. Bergner, J. Rösler, B. Gehrmann, and J. Klöwer: in *Proceedings of the 9th International Symposium on Superalloy 718 & Derivatives: Energy, Aerospace, and Industrial Applications*, Springer. 2018, pp. 489–99.
43. A. Baytaroglu: Chalmers University of Technology, 2022.
44. H. Bian, X. Xu, Y. Li, Y. Koizumi, Z. Wang, M. Chen, K. Yamanaka, and A. Chiba: *NPG Asia Mater.*, 2015, vol. 7, p. 212.
45. A. Baldan: *Review Progress in Ostwald Ripening Theories and Their Applications to the γ-Precipitates in Nickel-Base Superalloys Part II Nickel-Base Superalloys* .
46. R.L. Kennedy: *Proc. Int. Symp. Superalloys Var. Deriv.*, 2005. pp. 1–14.